

A High-Resolution Coupled Riverine Flow, Tide, Wind, Wind Wave, and Storm Surge Model for Southern Louisiana and Mississippi. Part I: Model Development and Validation

S. BUNYA,^{*,###} J. C. DIETRICH,^{*} J. J. WESTERINK,^{*} B. A. EBERSOLE,⁺ J. M. SMITH,⁺ J. H. ATKINSON,[#]
R. JENSEN,⁺ D. T. RESIO,⁺ R. A. LUETTICH,[@] C. DAWSON,[&] V. J. CARDONE,^{**} A. T. COX,^{**}
M. D. POWELL,⁺⁺ H. J. WESTERINK,^{*} AND H. J. ROBERTS[#]

^{*} Department of Civil Engineering and Geological Sciences, University of Notre Dame, Notre Dame, Indiana
⁺ Coastal Hydraulics Laboratory, U.S. Army Engineer Research and Development Center, Vicksburg, Mississippi

[#] Arcadis, Inc., Denver, Colorado

[@] Institute of Marine Sciences, University of North Carolina at Chapel Hill, Chapel Hill, North Carolina

[&] Institute for Computational Engineering and Sciences, The University of Texas at Austin, Austin, Texas

^{**} Oceanweather, Inc., Cos Cob, Connecticut

⁺⁺ NOAA/Atlantic Oceanographic and Meteorological Laboratories/Hurricane Research Division, Miami, Florida

(Manuscript received 11 December 2008, in final form 2 July 2009)

ABSTRACT

A coupled system of wind, wind wave, and coastal circulation models has been implemented for southern Louisiana and Mississippi to simulate riverine flows, tides, wind waves, and hurricane storm surge in the region. The system combines the NOAA Hurricane Research Division Wind Analysis System (H*WIND) and the Interactive Objective Kinematic Analysis (IOKA) kinematic wind analyses, the Wave Model (WAM) offshore and Steady-State Irregular Wave (STWAVE) nearshore wind wave models, and the Advanced Circulation (ADCIRC) basin to channel-scale unstructured grid circulation model. The system emphasizes a high-resolution (down to 50 m) representation of the geometry, bathymetry, and topography; nonlinear coupling of all processes including wind wave radiation stress-induced set up; and objective specification of frictional parameters based on land-cover databases and commonly used parameters. Riverine flows and tides are validated for no storm conditions, while winds, wind waves, hydrographs, and high water marks are validated for Hurricanes Katrina and Rita.

1. Introduction

Coastal Louisiana and Mississippi are especially prone to large hurricanes because of their geographic location in the north-central Gulf of Mexico. Between 1941 and 2008, the central Gulf was impacted by 16 major hurricanes including storms in 1941, 1957 (Audrey), 1964 (Hilda), 1965 (Betsy), 1969 (Camille), 1974 (Carmen), 1979 (Frederic), 1992 (Andrew), 1995 (Opal), 2002 (Lili), 2004 (Ivan), 2005 (Dennis, Katrina, and Rita), and most recently in 2008 (Gustav and Ike). It is estimated that this

region is more than twice as likely to see a major Gulf hurricane compared to the adjacent coasts of Texas and Florida (Resio 2007). Wind-driven coastal surge from these large hurricanes was the most important contributor to devastating regional flooding, although maximum high water levels were also influenced by atmospheric pressure, tides, riverine currents, waves, and rainfall.

The central Gulf is not only statistically susceptible to more frequent hurricanes, but portions of this varied geographic system are vulnerable to developing especially large storm surge for a given set of storm characteristics because of the local geographic configuration. In particular, the east bank of the Mississippi River in southeastern Louisiana is characterized by a protruding delta on the Mississippi–Alabama shelf; the river itself; barrier islands; extensive levee, raised road, and railroad systems; low-lying topography; and large interconnected shallow lakes. Many of these features tend to amplify surge as water is blown from both the east and the south

^{##} Current affiliation: Department of Systems Innovation, The University of Tokyo, Tokyo, Japan.

Corresponding author address: J. J. Westerink, Department of Civil Engineering and Geological Sciences, University of Notre Dame, 156 Fitzpatrick Hall, Notre Dame, IN 46556.
E-mail: jjw@nd.edu

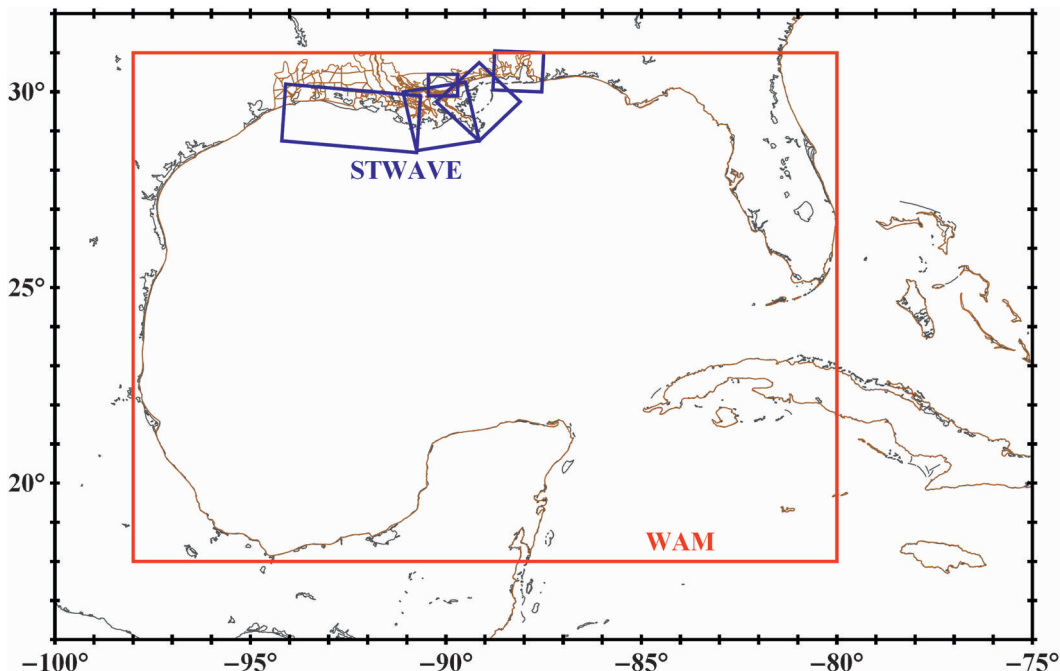


FIG. 1. WAM model domain shown in red and nested STWAVE model domains shown in blue. In order from west to east, the five STWAVE domains are W, S, LP, SE, and MS-AL, as described in Table 1.

onto the shelf and then blocked by the delta, river banks, levees, and railroad beds. The regional surge in the lower Mississippi River is often propagated up the river, reaching New Orleans within hours. While the state of Mississippi is topographically more varied than Louisiana, with shallow estuaries and low-lying riverine basins interspersed with higher areas including a system of barrier islands lying to the south, Mississippi is also dramatically affected by the Mississippi River’s protrusion onto the shallow continental shelf. In fact, Pass Christian, Mississippi, experienced the largest storm surge ever recorded in the United States during Hurricane Katrina (Ebersole et al. 2007). Finally, western Louisiana is characterized by an east–west coastline, large inland lakes, and extensive low-lying wetlands. These features tend to diminish surge heights because

only the southerly winds in the right center quadrant of the storm effectively push water against the coast, and the extensive low-lying wetlands may attenuate transient surges in this area.

To model coastal surge in this complex region, we must include all significant flow processes, accurately define the physical system, numerically resolve the system and the energetic flows, and apply accurate algorithms to solve the resulting mathematical model. The goal is to implement a modeling capability that represents the basic physics of the system as it is observed and does not require ad hoc model tuning of subgrid-scale coefficients, forcing functions, and/or boundary conditions.

The processes that affect storm surge inundation include winds, air–sea momentum transfer, atmospheric pressure, wind-driven waves, riverine flows, tides, and

TABLE 1. STWAVE grid names, the origin of the southeast corner in degrees latitude and longitude (northwest corner for the Lake Pontchartrain grid), orientation in degrees measured counterclockwise from the parallel that runs through the origin, and an indicator if the full or half plane version of STWAVE was run.

Grid	Name	Origin (λ, φ)	Orientation	x Cells	y Cells	STWAVE version	Used for Katrina	Used for Rita
Lake Pontchartrain	LP	$-90.4668^\circ, 30.4301^\circ$	270°	284	352	Full plane	✓	✓
Louisiana southeast	SE	$-88.1354^\circ, 29.9731^\circ$	141°	683	744	Half plane	✓	✓
Louisiana south	S	$-89.0945^\circ, 28.9617^\circ$	108°	825	839	Half plane	✓	✓
Mississippi and Alabama	MS-AL	$-87.6000^\circ, 30.0000^\circ$	90°	563	605	Half plane	✓	✓
Louisiana west	W	$-90.7332^\circ, 28.4633^\circ$	86°	980	1740	Half plane		✓

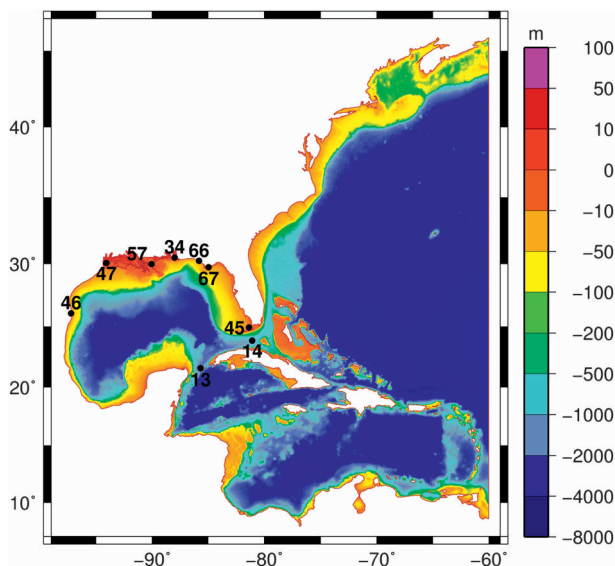


FIG. 2. ADCIRC SL15 model domain with bathymetry (m). Geographic locations of interest are indicated by the numbers identified in Table 2.

friction. Wind is the driving force of both wind waves and surge, and the characterization of the marine winds is paramount to obtaining accurate surge predictions. Wind wave generation and propagation, subsequent depth-limited breaking, and dissipation by vegetation in the nearshore or floodplain, and the associated transfer of the wind wave momentum through wave radiation stress gradient forcing, influence storm surge elevations and currents and modify the peak surge, the time of arrival of the peak surge, and drawdown. Water levels, currents, and wind waves affect the atmospheric boundary layer and the

air–sea momentum transfer while water levels and currents affect the generation and transformation of waves. Riverine flows not only affect overall water levels, but can also affect the propagation of wind waves, tides, and surge up the rivers. Although tides are modest in the region and dominated by less energetic diurnal tides, they modify water levels and can do so nonlinearly. We consider the full nonlinear interaction of these processes to simulate wave and water level conditions throughout the domain.

Tides, waves, and surge are influenced by both basin-scale and local-scale geometric features and flow gradients. Astronomical tides in the Gulf of Mexico are affected by basin-wide generation and shelf dissipation processes, while inland propagation of these tides is affected by the details of the connecting channels and marshes. Storm surge in Lake Pontchartrain depends not only on local setup but also on the high-volume inflows from Lake Borgne through the Rigolets and Chef Menteur pass, and over the interlake marshes. In turn, the Lake Pontchartrain–Lake Borgne storm surge flow exchange depends on the water pushed onto the Mississippi–Alabama shelf, wind wave breaking-induced setup, the level of attenuation of surge into inland Mississippi, and local geometry and bathymetry.

The complexity of the entire system must be accurately defined and computationally resolved in the numerical models in order for the growth, propagation, and attenuation of waves, surge, tides, and riverine flows to be modeled correctly. High grid resolution is necessary when high spatial gradients exist in the geometric and topographic features as well as in the waves, surface elevations, and currents. The emergence of high-density observational data such as lidar and satellite photography

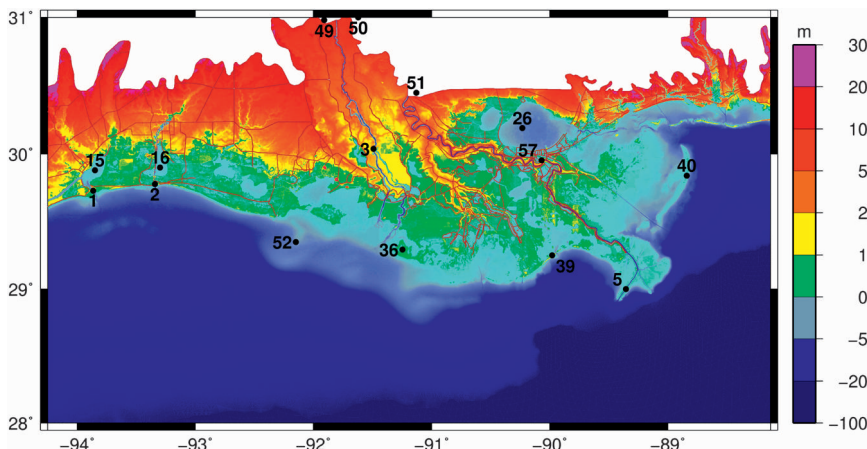


FIG. 3. Detail of the SL15 domain across southern Louisiana and Mississippi with bathymetry and topography [m relative to NAVD88 (2004.65)] with raised features such as levees, railroads, and highways shown in brown. Geographic locations of interest are indicated by numbers identified in Table 2.

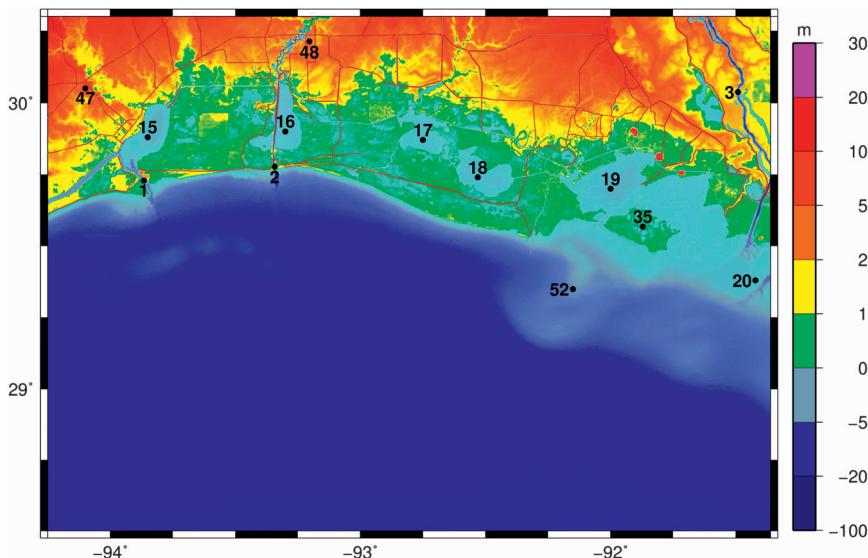


FIG. 4. As in Fig. 3, but across southwestern Louisiana.

has significantly improved the accurate characterization of topography, raised features, and surface roughness. In addition, dense soundings have improved the accurate characterization of the bathymetry.

In this paper, we describe the “SL15” storm surge model for Louisiana and Mississippi, which couples a sequence of well verified and validated wind, short-period wind wave, and coastal circulation models as an atmospheric–hydrodynamic modeling system. We independently validate each process with the available observational data, quantify differences between the component modeled and observational data and when possible estimate the uncertainty in the observational data itself. We stress that the validity of the coupled system relies on its ability to accurately represent the individual components and to then nonlinearly couple these components. We derive error estimates for the modeled river flows, tides, and Hurricane Katrina and Rita winds, waves, and surge levels. In a companion paper, we describe the detailed evolution and physics of winds, waves, surface elevation, and currents during Hurricanes Katrina and Rita (Dietrich et al. 2010).

2. Coupled wind, wind wave, tide, riverine flow model system

a. Kinematic winds

For hindcasting historical storms, we define wind fields using objectively analyzed measurements. Observational data comes from anemometers, airborne and land-based Doppler radar, airborne stepped-frequency microwave radiometer, buoys, ships, aircraft, coastal stations, and satellite measurements. For Katrina, the measured

winds in the inner core are assimilated using the National Oceanic and Atmospheric Administration (NOAA) Hurricane Research Division Wind Analysis System (H*WIND) (Powell et al. 1996, 1998) and are then blended with Gulf-scale winds using an Interactive Objective Kinematic Analysis (IOKA) system (Cox et al. 1995; Cardone et al. 2007). H*WIND composites observations of wind velocity relative to the storm’s center and transforms them to a common reference condition of 10-m height, peak 1-min-averaged “sustained” wind speed, and marine exposure. A special set of H*WIND reanalyzed snapshots are available for Katrina (Powell et al. 2008). Peripheral winds are derived from the National Centers for Environmental Prediction–National Center for Atmospheric Research (NCEP–NCAR) reanalysis project (Kalnay et al. 1996). Before inner-core and peripheral wind fields are blended, the inner core peak sustained winds are transformed to 30-min-average wind speeds using a gust model consistent with the H*WIND system. A final step is to inject local marine data, adjusted to a consistent 10-m elevation and neutral stability using the IOKA system. Lagrangian-based interpolation is used to produce the final wind fields on a regular $0.05^\circ \times 0.05^\circ$ grid with snapshots every 15 min. Hurricane Rita inner-core wind fields are based mainly on TC96 mesoscale model (Thompson and Cardone 1996) solutions blended as described above into peripheral fields using IOKA (Cardone and Cox 2007; Cardone et al. 2007). Both hurricanes’ pressure fields used to drive the atmospheric pressure term in the circulation model are derived using a widely adopted parametric relationship (Holland 1980).

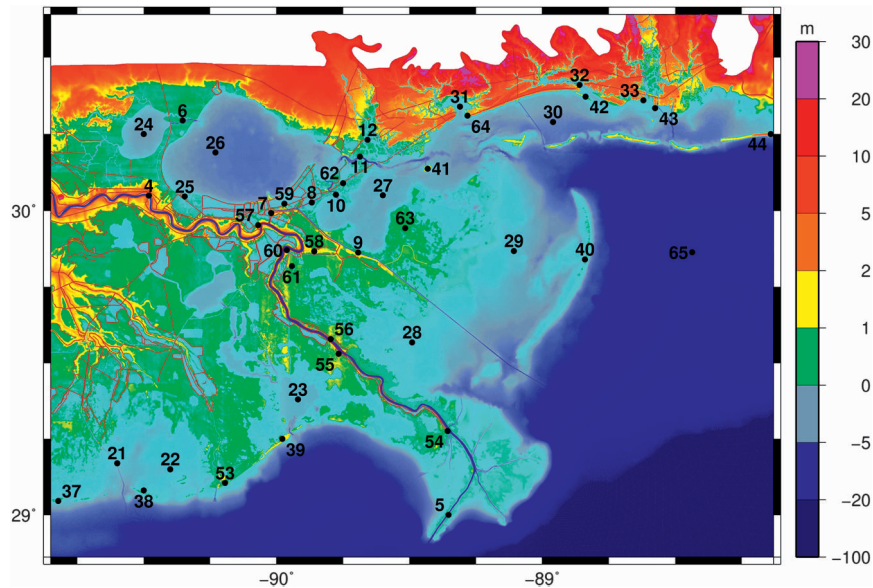


FIG. 5. As in Fig. 3, but across southeastern Louisiana and Mississippi.

b. Deep-water wind wave model WAM

The Wave Model (WAM) is run to generate deep-water wave fields and directional spectra in a Gulf of Mexico domain. WAM is a third-generation discrete spectral wave model that solves the wave action balance equation and includes source-sink terms, atmospheric input, nonlinear wave–wave interactions, white-capping, bottom friction, and depth-limited wave breaking. The spatial and temporal variation of wave action in frequency and direction is solved over a fixed spatial grid (Komen et al. 1994). WAM has recently undergone major revisions to source term specification, multigrid nesting, and depth-limited breaking (Gunther 2005). The model computes directional wave spectra for 28 discrete frequency bands, and 24 directional bands centered every 15° .

The WAM model domain, shown in Fig. 1, extends over the entire Gulf of Mexico with a grid at 0.05° resolution. It is assumed that the wind waves are generated in the Gulf and that wave energy entering the Gulf and reaching the area of interest through the Florida and Yucatan Straits is minimal. Wave data within and outside of the Gulf indicates that the dominant wave energy is generated within the Gulf, along with the hurricane. The WAM model allows wave energy to propagate out of the Gulf through the Yucatan and Florida straits. The water depth is derived from the General Bathymetric Chart of the Oceans (British Oceanographic Data Centre 2003). The H*WIND–IOKA 30-min-averaged wind fields are linearly interpolated in time and space onto the WAM grid.

c. Nearshore wave model STWAVE

The nearshore wind wave model Steady-State Irregular Wave (STWAVE; Smith 2000; Smith et al. 2001; Smith and Smith 2001; Thompson et al. 2004) is used to generate and transform waves to the shore. STWAVE solves the steady-state conservation of spectral action balance along backward-traced wave rays. The source terms include wind input, nonlinear wave–wave interactions, dissipation within the wave field, and surf-zone breaking. The computed terms include wave propagation and source terms representing energy growth and decay in the spectrum. The assumptions made in STWAVE include a mild bottom slope; negligible wave reflection; steady waves, currents, and winds; linear refraction and shoaling, and a depth-uniform current. STWAVE can be implemented as either a half-plane model, where only waves propagating toward the coast are represented, or a full-plane model, allowing generation and propagation in all directions. Wave breaking in the surf zone limits the maximum wave height based on the local water depth and wave steepness.

Four or five STWAVE grids are used to simulate nearshore and coastal floodplain wind wave propagation and attenuation. These grids, also shown in Fig. 1 and summarized in Table 1, extend across coastal Louisiana, Mississippi, and Alabama. The spatial resolution of each STWAVE grid is 200 m. Bathymetry for all grids is interpolated from the Advanced Circulation (ADCIRC) model grid.

Open-water boundary conditions are obtained by extracting the wave energy spectra from the WAM

TABLE 2. Geographic location by type and number shown in Figs. 2–5.

Rivers and channels	
1	Sabine Pass
2	Calcasieu Shipping Channel
3	Atchafalaya River
4	Mississippi River
5	Southwest Pass
6	Pass Manchac
7	Inner Harbor Navigation Canal (IHNC)
8	Gulf Intracoastal Waterway (GIWW)
9	Mississippi River Gulf Outlet (MRGO)
10	Chef Menteur Pass
11	Rigolets
12	Pearl River
13	Yucatan Strait
14	Florida Strait
Bays, lakes, and sounds	
15	Sabine Lake
16	Calcasieu Lake
17	Grand Lake
18	White Lake
19	Vermilion Bay
20	Atchafalaya Bay
21	Terrebonne Bay
22	Timbalier Bay
23	Barataria Bay
24	Lake Maurepas
25	Bayou Labranche
26	Lake Pontchartrain
27	Lake Borgne
28	Breton Sound
29	Chandeleur Sound
30	Mississippi Sound
31	St. Louis Bay
32	Biloxi Bay
33	Pascagoula Bay
34	Mobile Bay
Islands	
35	Marsh Island
36	Point au Fer Island
37	Isle Dernieres
38	Timbalier Island
39	Grand Isle
40	Chandeleur Islands
41	Half Moon Island
42	Deer Island
43	Singing River Island
44	Dauphin Island
45	Florida Keys
Places	
46	Port Isabel, TX
47	Beaumont, TX
48	Lake Charles, LA
49	Simmesport, LA
50	Tarbert Landing
51	Baton Rouge, LA

TABLE 2. (Continued)

52	Tiger Shoal, Trinity Shoal
53	Port Fourchon, LA
54	Venice, LA
55	Socola, LA
56	Point a la Hache, LA
57	New Orleans, LA
58	St. Bernard
59	New Orleans East
60	English Turn
61	Caernarvon Marsh
62	CSX Railroad
63	Biloxi Marsh
64	Pass Christian, MS
65	Mississippi-Alabama Shelf
66	Panama City Beach, FL
67	Apalachicola, FL

solutions at the STWAVE boundary nodes. The wind fields are interpolated from the ADCIRC wind fields, which apply land effects to the H*WIND/IOKA marine wind fields. STWAVE is run at 30-min intervals for 2 days. The STWAVE computations include preliminary water levels interpolated from ADCIRC simulations forced only with wind, atmospheric pressure, riverine flows, and tides. Radiation stresses computed with STWAVE are added as input to a subsequent ADCIRC simulation.

d. ADCIRC model

The last component of the system is the ADCIRC unstructured coastal ocean circulation model, which is applied to compute surface water elevation and currents. The ADCIRC model solves the depth-integrated barotropic shallow-water equations in spherical coordinates using a finite-element solution (Luettich and Westerink 2004; Atkinson et al. 2004; Dawson et al. 2006; Westerink et al. 2008). The solution maintains both accuracy and robustness when applied to the wide range of scales of motion and wide range of hydrodynamic balances that exist when computing flows in the deep ocean transitioning to flows in inlets, floodplains, and rivers. The use of an unstructured grid allows for high localized grid resolution where solution gradients are large, and low grid resolution where solution gradients are small, minimizing both local and global error norms for a given computational cost.

e. SL15 domain and grid

The ADCIRC SL15 model domain, shown in Fig. 2, is an evolution of the earlier EC2001 U.S. East Coast and

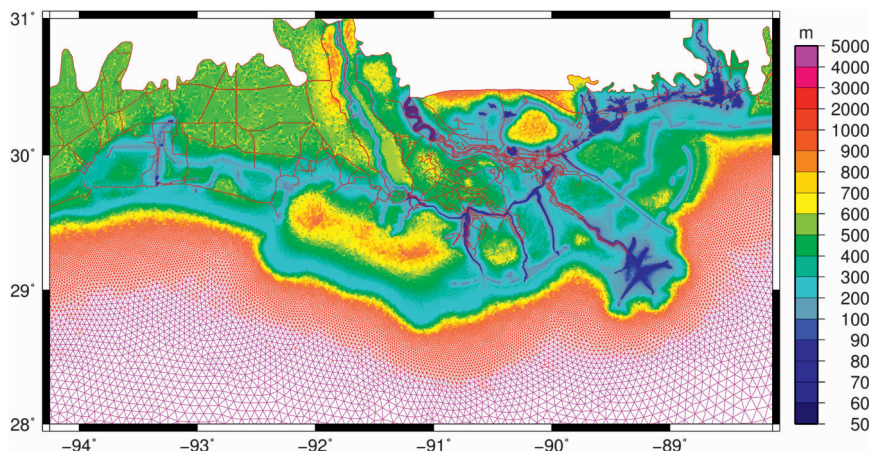


FIG. 6. Detail of the SL15 grid across southern Louisiana and Mississippi with finite-element sizes shown in meters.

Gulf of Mexico astronomical tide model and the S08 southern Louisiana storm surge model (Blain et al. 1994; Mukai et al. 2002; Westerink et al. 2008). These models incorporate the western North Atlantic Ocean, the Gulf of Mexico, and the Caribbean Sea to allow for full dynamic coupling between oceans, continental shelves, and the coastal floodplain without necessitating that these complicated couplings be defined in the boundary conditions. The SL15 model extends the coverage of these earlier models to include all the floodplains of southern Louisiana and Mississippi. In addition, improved definitions of features, surface roughness, wave radiation stress, and grid resolution are incorporated. The highly resolved floodplain in the SL15 model extends from Beaumont, Texas, to Mobile Bay, Alabama. Areas in Texas and Alabama are included to allow storm surge that affects Louisiana and Mississippi to realistically attenuate and laterally spread into the adjacent states. In southern Louisiana and Mississippi, the northern land boundary extends along the 10–20-m elevation contours or major hydraulic controls. Details of the domain with bathymetry and topography as well as levees and raised roadways across southern Louisiana can be seen in Figs. 3–5 with geographic places of interest listed in Table 2.

The computational grid resolves the tidal, wind, atmospheric pressure, and riverine flow forcing functions and flow processes from the ocean basins to the coastal floodplain. Effective resolution of tidal and hurricane response within the basins and on the shelf is determined by tidal wavelength, topographic length scale criteria, and hurricane size criteria (Westerink et al. 1994; Blain et al. 1998; Hagen et al. 2001). The grid applies localized refinement of the coastal floodplains and of the important hydraulic features, down to 50 m in critical channels

and conveyances, as shown in Fig. 6. We accommodate the STWAVE forcing function by adding a swath of 50–200-m grid resolution along the coast, over barrier islands, and around Lake Pontchartrain where there are significant gradients in the wave radiation stresses and where forcing of surge through wave transformation is the largest. Barrier islands also need high grid refinement to resolve the very high currents that develop when these features are overtopped.

The SL15 computational grid contains 2 409 635 nodes and 4 721 496 elements. Grid resolution varies from

TABLE 3. Manning-*n* values for LA-GAP classification.

LA-GAP class	Description	Manning <i>n</i>
1	Fresh marsh	0.055
2	Intermediate marsh	0.050
3	Brackish marsh	0.045
4	Saline marsh	0.035
5	Wetland forest—deciduous	0.140
6	Wetland forest—evergreen	0.160
7	Wetland forest—mixed	0.150
8	Upland forest—deciduous	0.160
9	Upland forest—evergreen	0.180
10	Upland forest—mixed	0.170
11	Dense pine thicket	0.180
12	Wetland scrub/shrub—deciduous	0.060
13	Wetland scrub/shrub—evergreen	0.080
14	Wetland scrub/shrub—mixed	0.070
15	Upland scrub/shrub—deciduous	0.070
16	Upland scrub/shrub—evergreen	0.090
17	Upland scrub/shrub—mixed	0.080
18	Agriculture—crops—grass	0.040
19	Vegetated urban	0.120
20	Nonvegetated urban	0.120
21	Wetland barren	0.030
22	Upland barren	0.030
23	Water	0.02–0.045

TABLE 4. Manning-*n* values for MS-GAP classification.

MS-GAP class	Description	Manning <i>n</i>
1	Agriculture	0.060
2	Freshwater	0.025
3	Aquaculture	0.045
4	Estuarine water	0.025
6	Farmed wetlands	0.035
7	Estuarine emergent	0.050
8	Estuarine woody	0.060
9	Palustrine emergent	0.055
10	Bottomland hardwood	0.140
11	Riverine swamp	0.060
12	Pine savannah	0.160
13	Freshwater shrub/scrub	0.070
14	Palustrine nonvegetated	0.030
15	Transportation	0.032
16	High density urban	0.150
24	Urban freshwater	0.025
25	Wet soil/water/shadow	0.040
26	Urban pine	0.180
27	Urban hardwood	0.160
28	Urban low herbaceous	0.070
29	Urban grassy/pasture	0.035
30	Bare urban I	0.120
31	Bare urban II	0.120
32	Clear cuts	0.036
50	Low-density pine	0.160
51	Medium-density pine	0.180
52	High-density pine	0.200
53	Medium-density hardwood	0.170
54	High-density hardwood	0.170
55	Mixed forest	0.160
56	Recent harvest	0.052
57	Cypress/tupelo	0.180
60	Agriculture (see class No. 1)	0.060
61	Grassy/pasture/range	0.042
62	Low herbaceous vegetation	0.047
63	Evergreen shrub	0.080
71	Wetland	0.045
80	Bare	0.030
81	Sand bar/beach	0.030

TABLE 5. Manning-*n* values for 1992 NLCD classification.

NLCD class	Description	Manning <i>n</i>
11	Open water	0.020
12	Ice/snow	0.022
21	Low residential	0.120
22	High residential	0.121
23	Commercial	0.050
31	Bare rock/sand	0.040
32	Gravel pit	0.060
33	Transitional	0.100
41	Deciduous forest	0.160
42	Evergreen forest	0.180
43	Mixed forest	0.170
51	Shrub land	0.070
61	Orchard/vineyard	0.100
71	Grassland	0.035
81	Pasture	0.033
82	Row crops	0.040
83	Small grains	0.035
84	Fallow	0.032
85	Recreational grass	0.030
91	Woody wetland	0.140
92	Herbaceous wetland	0.035

24 km in the Atlantic Ocean to about 50 m in Louisiana and Mississippi. Unstructured grids can resolve the critical features and the associated local flow processes with orders of magnitude fewer computational nodes than a structured grid.

f. SL15 bathymetry and topography

Geometry, topography, and bathymetry in the SL15 model are defined to replicate the prevailing conditions in August 2005 prior to Hurricane Katrina, with the exception of some of the barrier islands and the area between Lake Pontchartrain and Lake Borgne, which are included as post-Katrina September 2005 configurations. Open-ocean and shelf bathymetric depths are

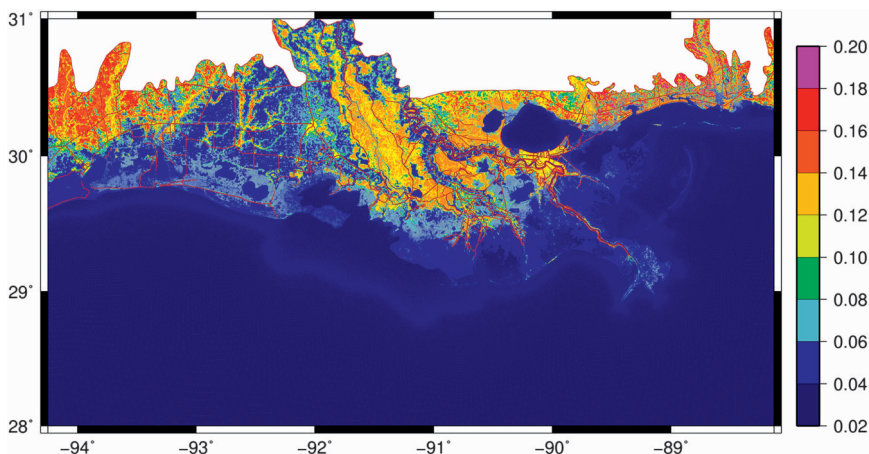


FIG. 7. Detail of the applied Manning *n* roughness coefficients for southern Louisiana.

TABLE 6. ADCIRC model run segments for the river, tide, Hurricanes Katrina and Rita validation runs in days from the start of the simulation or in UTC time (hour/day/month). Duration of the application of the river ramp, time for the rivers to reach equilibrium, the duration of the tidal forcing ramp, the time for the tides to reach dynamic equilibrium, the duration of the wind and wave forcing are given.

Simulation	River ramp	River equilibrium	Tidal forcing ramp	Tidal forcing equilibrium	Wind forcing	Wave forcing	Run completion
River validation	0.0–0.5	0.5–5.0					5.0
Tidal validation	0.0–0.5	0.5–2.0	2.0–20.0	20.0–45.0			45.0–105.0
Hurricane Katrina	0000–1200 UTC 7 Aug	1200 UTC 7 Aug–0000 UTC 9 Aug	0000 UTC 9 Aug–0000 UTC 19 Aug	0000 UTC 19 Aug–0000 UTC 25 Aug	0000 UTC 25 Aug–0000 UTC 31 Aug	1215 UTC 28 Aug–1145 UTC 30 Aug	0000 UTC 25 Aug–0000 UTC 1 Sep
Hurricane Rita	0000–1200 UTC 31 Aug	1200 UTC 31 Aug–0000 UTC 2 Sep	0000 UTC 2 Sep–0000 UTC 12 Sep	0000 UTC 12 Sep–0000 UTC 18 Sep	0000 UTC 18 Sep–0000 UTC 25 Sep	1830 UTC 22 Sep–1800 UTC 24 Sep	0000 UTC 18 Sep–0000 UTC 29 Sep

interpolated in order of preference from NOAA’s bathymetric sounding database, the Digital Nautical Charts database, and the 5-minute gridded elevations/bathymetry for the world (ETOPO5) database (National Ocean Service 1997; U.S. Department of Defense 1999; National Geophysical Data Center 1988; Mukai et al. 2002). Inland bathymetry is taken from regional bathymetric surveys from the U.S. Army Corps of Engineers New Orleans District (USACE-MVN).

Topography in the floodplain is obtained predominantly from the Atlas and the Mississippi Coastal Analysis Lidar Projects (Louisiana State University 2004; URS 2008). Where no data is available in the wetlands, the Louisiana Gap Analysis Project (LA-GAP) land-cover data (Hartley et al. 2000) is applied with estimated topographic heights of 0.80 m for marshland and –0.40 m for water. The U.S. Geological Survey (USGS) post-Katrina lidar data is applied to the Chandeleur Islands, and USACE post-Katrina lidar data is used for the Mississippi Sound Islands with the exception of Half Moon Island, Deer Island, and Singing River Island, where Mississippi Automated Resource Information System (MARIS) data is used (Mississippi Automated Resource Information System 2006). Levee and road systems that are barriers to flood propagation are features that fall below the defined grid scale, and represent a nonhydrostatic flow handled as a subgrid-scale weir (Westerink et al. 2008). All federal levees, many local and private levees, and road heights are defined using the USACE-MVN surveys. Road and railroad crown heights in Louisiana are generally taken from the Atlas lidar surveys. Note that the CSX railway between the Rigolets and Chef Menteur Pass in particular is important as a control in the flow between Lake Borgne and Lake Pontchartrain. According to the Atlas lidar surveys, the railway has a height of about 3.5 m. However, CSX railway personnel involved in the re-

construction indicated that the gravel bed was washed out during the storm and that the remaining compacted bed was at no more than 2 m, the elevation incorporated into the model. In addition, US 90 sustained some damage and estimates of the lowered values are made.

g. Vertical datum, LMSL, and steric water level adjustments

The North American Vertical Datum of 1988 (NAVD88) updated to the 2004.65 epoch, NAVD88 (2004.65) is used as the vertical reference. Topography is available relative to the original epoch, NAVD88, while federal levees and high water mark (HWM) data are available relative to NAVD88 (2004.65). Garster et al. (2007) computed the adjustment from local mean sea level (LMSL) to NAVD88 (2004.65) at 12 stations throughout southern Louisiana. The average adjustment at the 11 reliable stations is 0.134 m. Additionally, an examination of the datums at NOAA stations in the region reveals that LMSL regionally lies above mean lower low water (MLLW) by 0.152 m. Thus, bathymetric data, referenced to MLLW, has been regionally adjusted to NAVD88 (2004.65) by adding 0.018 m.

The computations themselves are referenced to NAVD88 (2004.65) by adding 0.134 m to the baseline LMSL reference of the model. Because the computations are barotropic, it is also necessary to account for

TABLE 7. River flow rates (m³ s⁻¹) for the various simulations.

Case	Mississippi River	Atchafalaya River
River validation	4730–33 110	1980–13 860
Tidal validation	4730	1980
Hurricane Katrina	4730	1980
Hurricane Rita	5125	2240

TABLE 8. Principal tidal constituents with periods (hours), tidal potential constants (m), and associated effective earth elasticity factors.

Species, j	n	Constituent	Name	T_{jn} (h)	C_{jn} (m)	α_{jn}
1	1	K_1	Luni-solar	23.934 470	0.141 565	0.736
	2	O_1	Principal lunar	25.819 342	0.100 514	0.695
	3	Q_1	Elliptical lunar	26.868 357	0.019 256	0.695
2	1	M_2	Principal lunar	12.420 601	0.242 334	0.693
	2	S_2	Principal solar	12.000 000	0.112 841	0.693
	3	N_2	Elliptical lunar	12.658 348	0.046 398	0.693
	4	K_2	Luni-solar	11.967 235	0.030 704	0.693

the annual fluctuation in sea level due to thermal expansion of the upper layers of the Gulf of Mexico and by other effects. NOAA long-term stations at Dauphin Island, Mississippi, Grand Isle, Louisiana, and Sabine Pass, Texas, indicate that the increase in surface elevations is bimodal with station-averaged maximum mid-September water levels increasing to 0.158 m above the annual average (more information is available online at <http://tidesandcurrents.noaa.gov/sltrends/sltrends.html>). This expansion is also captured in harmonically decomposed tidal records by the long-term S_a and S_{sa} constituents, which show an average regional combined amplitude of 0.15 m with a standard deviation of 0.03 m. To make the seasonal sea surface adjustment for a specific storm, the regional long-term sea level station data is used at the date of landfall. Thus for Katrina, which occurred in late August, sea surface level increase above the annual average is regionally estimated as 0.10 m above LMSL, while for Rita, which made landfall on 24 September, the estimated increase is 0.15 m. Initial water levels in the model are therefore raised at the start of the computation with the combined average regional difference between LMSL and NAVD88 (2004.65) in addition to the steric increase. For Katrina, this adjustment equals $0.13 \text{ m} + 0.10 \text{ m} = 0.23 \text{ m}$. For Rita the adjustment equals $0.13 \text{ m} + 0.15 \text{ m} = 0.28 \text{ m}$.

h. Hydraulic friction

Bottom friction is computed by the standard quadratic parameterization of bottom stress using a Manning n formulation. Nodal Manning n coefficients are spatially assigned using land-cover definitions from the USGS LA-GAP in Louisiana, USGS Mississippi Gap Analysis Project (MS-GAP), and the USGS National Land Cover Data (NLCD) in Texas and Alabama (Hartley et al. 2000; Villea 2005; Vogelmann et al. 2001). The GAP data are preferred because the classification system, particularly in wetlands, is more detailed than the NLCD data. The Manning n associated with these land classifications, presented in Tables 3–5, are selected or interpolated from standard hydraulic literature (Chow 1959; Barnes 1967;

Arcement and Schneider 1989). For the open ocean, large inland lakes, sheltered estuaries, deep straight inlet channels, deep meandering rivers, and shallow meandering channels, n is assigned 0.02, 0.02, 0.025, 0.025, 0.025, and 0.045, respectively. Figure 7 shows the applied Manning n values in southern Louisiana. The bottom friction coefficient C_f has a defined lower limit equal to 0.003 in ocean and shelf waters in order to be consistent with Mukai et al. (2002). Lateral eddy viscosity is uniformly set to $5 \text{ m}^2 \text{ s}^{-1}$ in water and $50 \text{ m}^2 \text{ s}^{-1}$ on land.

i. Riverine forcing

At the Mississippi River at Baton Rouge, Louisiana, and at the Atchafalaya River at Simmesport, Louisiana, inflows are specified with a wave radiation boundary

TABLE 9. The 1992 NLCD nominal land roughness values, $z_{0\text{-land}}$. The *Class 95 is constructed from the GAP data for Louisiana. The NLCD did not have coverage for cypress wetland forest; therefore GAP datasets were merged into the NLCD and the cypress forest land type was imposed on top of the NLCD data.

NLCD class	Description	$z_{0\text{-land}}$
11	Open water	0.001
12	Ice/snow	0.012
21	Low residential	0.330
22	High residential	0.500
23	Commercial	0.390
31	Bare rock/sand	0.090
32	Gravel pit	0.180
33	Transitional	0.180
41	Deciduous forest	0.650
42	Evergreen forest	0.720
43	Mixed forest	0.710
51	Shrub land	0.120
61	Orchard/vineyard	0.270
71	Grassland	0.040
81	Pasture	0.060
82	Row crops	0.060
83	Small grains	0.050
84	Fallow	0.040
85	Recreational grass	0.050
91	Woody wetland	0.550
92	Herbaceous wetland	0.110
95*	Cypress forest	0.550

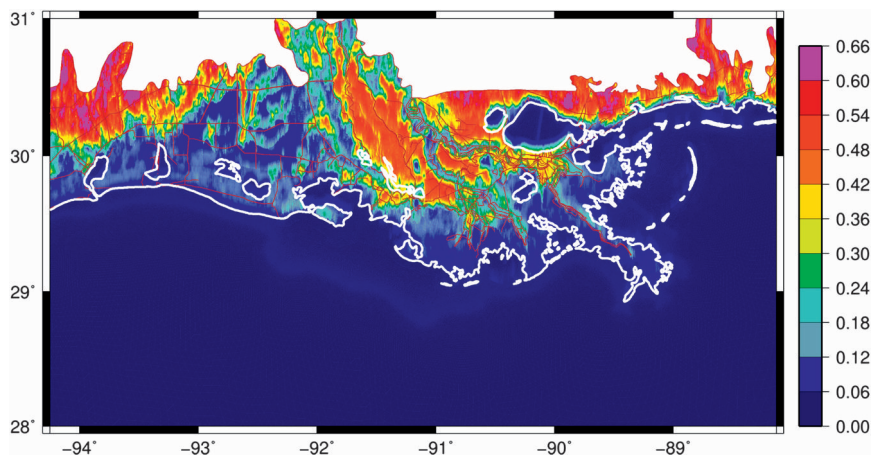


FIG. 8. Sample of the applied directional wind reduction factor for uniform steady southerly winds for southern Louisiana. The coastline is outlined in white.

condition that ensures that neither surges nor tides artificially reflect back into the computational domain (Westerink et al. 2008). The river condition is spun up specifying a steady flow with no other forcings in the model, using a 0.5-day hyperbolic ramp, and running for 2.0–4.5 days to reach a dynamic steady state as summarized in Table 6. After this, the river radiation boundary condition is applied and other forcings are spun up. River flow rates for the simulations are specified in Table 7.

j. Tidal forcing

After the rivers have reached equilibrium, tides are spun up in the circulation model. Tides are forced on the Atlantic open-ocean boundary along the 60°W meridian with the seven dominant astronomical tidal constituents and include the diurnal O_1 , K_1 , and Q_1 constituents and the semidiurnal M_2 , N_2 , S_2 , and K_2 constituents, using data from Le Provost’s FES95.2 global model (Le Provost et al. 1998; Mukai et al. 2002). In addition, tidal

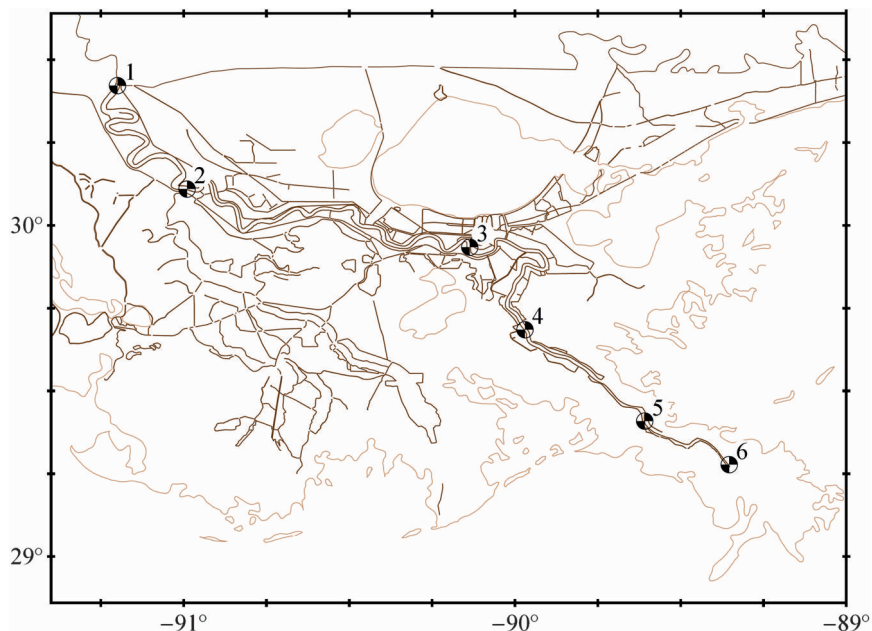


FIG. 9. Locations of the six USACE stations with stage–flow relationships that were compared to the computed water levels in Fig. 10. In numerical order, the six stations are Baton Rouge, Donaldsonville, New Orleans, Alliance, Empire, and Venice.

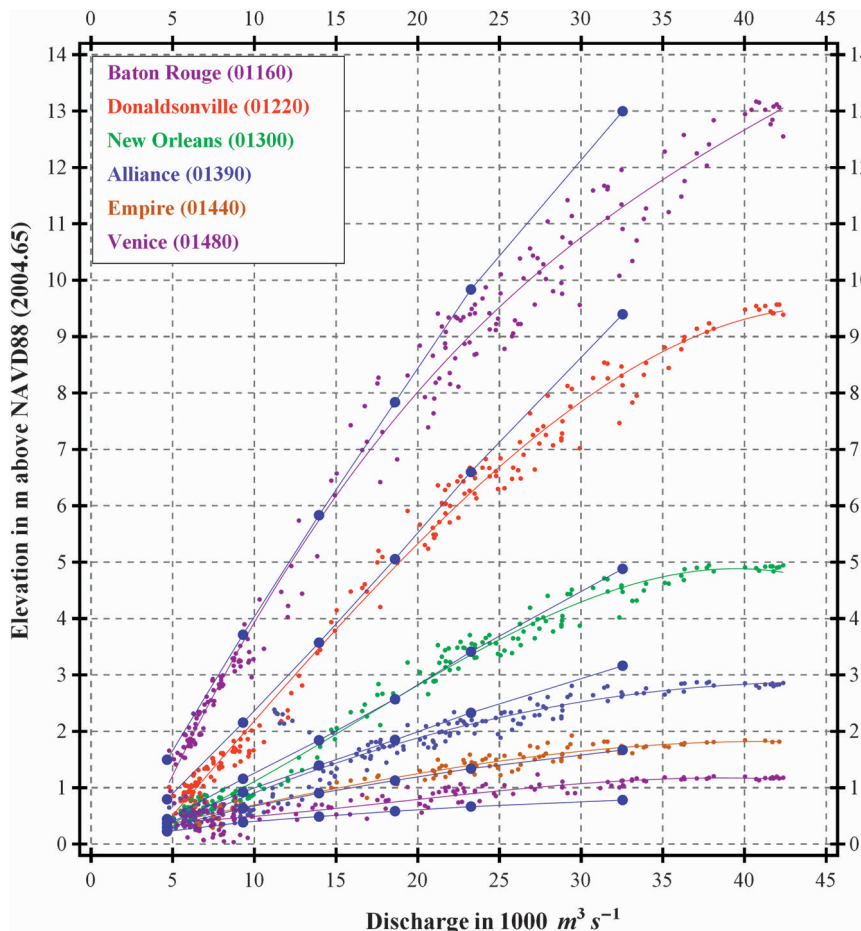


FIG. 10. Stage-flow relationships at six USACE stations along the Mississippi River. Measured data is shown as scatter points with associated best-fit curves. The predicted data is shown as connected blue dots.

potential functions are forced within the model domain for the same constituents. Periods, tidal potential constants, and the earth elasticity factors, which reduce the magnitude of the tidal potential forcing due to the earth tides, are listed in Table 8 (Hendershott 1981). Finally, the nodal factor and equilibrium argument for boundary and interior domain forcing tidal constituents are based on the starting time of the simulation. The resonant characteristics of the Gulf of Mexico and Caribbean Sea require a period of model simulation or spinup in order for the initial transients to physically dissipate and dynamically correct tides to be generated. Tidal spinup ramps and run times are detailed in Table 6.

k. Atmospheric and wave forcing

The IOKA-H*WIND wind field analyses provide marine wind exposure at 10-m height and 30-min-averaged winds. The wind surface stress is computed by a standard

quadratic air-sea drag law. The air-sea drag coefficient is defined by Garratt’s drag formula, which is based largely on 10-min-averaged wind data (Garratt 1977). The IOKA-H*WIND winds are therefore adjusted to 10-min averages by noting that shorter sampling periods lead to higher-averaged winds and increasing them by

TABLE 10. Summary of average absolute differences (m) for the stage-flow relationships shown in Fig. 10.

Station name	Station ID	Avg absolute diff, SL15 to best-fit curve	Avg absolute diff, measured data to best-fit curve
Baton Rouge	01160	0.583 413	0.343 085
Donaldsonville	01220	0.377 853	0.216 160
New Orleans	01300	0.120 856	0.142 391
Alliance	01390	0.181 827	0.180 448
Empire	01440	0.043 808	0.085 810
Venice	01480	0.181 197	0.112 920

TABLE 11. NOAA stations used in the NOAA-measured to SL15-computed difference analysis for tidal constituents. The station IDs marked with asterisks (*) indicate stations whose longitude and latitude were shifted slightly in the ADCIRC SL15 model.

State	Station ID	Station name	Lon (°)	Lat (°)	
FL	8723962*	Key Colony Beach	-81.016 667	24.710 000	
	8724580	Key West	-81.808 333	24.553 333	
	8724698	Loggerhead Key	-82.920 000	24.631 667	
	8725110	Naples	-81.806 667	26.130 000	
	8726724	Clearwater Beach	-82.831 667	27.978 333	
	8727520	Cedar Key	-83.031 667	29.135 000	
	8728130	St Marks Lighthouse	-84.178 333	30.078 333	
	8728360	Turkey Point	-84.511 667	29.915 000	
	8729210	Panama City Beach	-85.878 333	30.213 333	
	8729678	Navarre Beach	-86.865 000	30.376 667	
	MS-AL	8735180*	Dauphin Island	-88.068 000	30.250 000
		8735181*	Dauphin Island Hydro	-88.068 000	30.250 000
		8737048	Mobile	-88.043 333	30.708 333
		8741196	Pascagoula Point	-88.533 333	30.340 000
8741533*		Pascagoula NOAA Laboratory	-88.565 263	30.358 333	
8742221*		Horn Island	-88.666 667	30.240 000	
8743281		Ocean Springs	-88.798 333	30.391 667	
8744117*		Biloxi	-88.903 333	30.412 408	
8745557		Gulfport Harbor	-89.081 667	30.360 000	
8747437		Bay Waveland Yacht Club	-89.325 000	30.325 000	
8747766		Waveland	-89.366 667	30.281 667	
LA	8760551	South Pass	-89.140 000	28.990 000	
	8760922	Pilots Station East, SW Pass	-89.406 667	28.931 667	
	8760943	SW Pass	-89.418 333	28.925 000	
	8761720*	Grand Isle	-89.962 380	29.269 130	
	8761724*	Grand Isle East Point	-89.962 380	29.269 130	
	8761927*	New Canal Station	-90.110 150	30.027 630	
	8762075*	Port Fourchon	-90.209 420	29.114 220	
	8762372	East Bank	-90.368 333	30.050 000	
	8762482	West Bank	-90.418 333	29.776 667	
	8764227	Lawma, Amerada Pass	-91.338 333	29.448 333	
	8764311	Eugene Island	-91.385 000	29.371 667	
	8765251	Cypremort Point	-91.880 000	29.713 333	
	8766072	Freshwater Canal Locks	-92.305 000	29.713 333	
	8767816*	Lake Charles	-93.224 430	30.223 510	
	8768094	Calcasieu Pass	-93.343 333	29.765 000	
TX	8770475	Port Arthur	-93.930 000	29.866 667	
	8771510	Galveston Pleasure Pier	-94.788 333	29.285 000	
	8775870	Corpus Christi	-97.216 667	27.580 000	
	8779770	Port Isabel	-97.215 000	26.060 000	

a factor of 1.09 as recommended by Cardone. Cardone's factor leads to almost identical 10-min winds as would be obtained by converting H*WIND peak 1-min winds to 10-min winds using Powell's recommended conversion factor of 0.89 (Powell et al. 1996). The drag coefficient is limited to 0.0035 to represent sheeting processes. Powell et al. (2003) found upper-limit values based on GPS dropwindsondes as low as 0.0025 although there appears to be strong quadrantal variation, the limit may be higher in outer portions of the storm and values in shallow shelf waters are only now being obtained.

The ADCIRC model corrects the IOKA-H*WIND marine winds to account for land roughness by making directional adjustments to the marine winds depending

on upwind roughness, level of local inundation, and the presence of tree canopies (Westerink et al. 2008). The directional wind reduction is based on the USGS NLCD supplemented with GAP land-cover classification raster maps for areas identified as cypress forest, combined with land roughness lengths in Table 9. Wind boundary layer readjustments depend upon roughness conditions upwind of the location. Figure 8 shows sample directional roughness coefficients for steady uniform southerly winds. Furthermore, as inundation takes place, the land roughness elements are submerged and the drag is reduced. Finally, canopied areas are defined where there are deciduous forests, evergreen forests, mixed forests, woody wetlands, or

TABLE 12. SL15 model harmonic constituents used to decompose model time histories into harmonic constituents.

Tidal constituent	Tidal description	T_{in} (h)
Steady	Overtide	
MN	Compound	661.309 205
SM	Compound	354.367 052
KO	Compound	327.858 999
O_1	Principal lunar	25.819 342
K_1	Luni-solar	23.934 470
Q_1	Elliptical lunar	26.868 357
MNS_2	Compound	13.127 267
$2MS_2$	Compound	11.606 952
N_2	Elliptical lunar	12.658 348
K_2	Luni-solar	11.967 235
M_2	Principal lunar	12.420 601
$2MN_2$	Compound	12.191 620
S_2	Principal solar	12.000 000
$2SM_2$	Compound	11.355 899
MN_4	Compound	6.269 174
M_4	Overtide	6.210 301
MS_4	Compound	6.103 339
$2MN_6$	Compound	4.166 284
M_6	Overtide	4.140 200
MSN_6	Compound	4.117 870
M_8	Overtide	3.105 150
M_{10}	Overtide	2.484 120

cypress forests. Canopies are assumed to be so high that no water overtops them and thick enough for wind not to penetrate them.

The wind and pressure fields snapshots are applied every 15 min during the periods listed in Table 6 and are linearly interpolated in time between snaps. The STWAVE wave radiation stress fields are read every 30 min during the periods listed in Table 6 and are linearly interpolated in time and space.

1. System performance

The five STWAVE grids and the ADCIRC SL15 grid were run on a CRAY XT3 with 2.6 GHz Opteron processors (Sapphire; see online at <http://www.ercd.hpc.mil>). The five STWAVE grids were run with a relatively large time interval of 1800 s, and they required 2484 s day^{-1} of simulation on 96 computational cores. The ADCIRC SL15 grid was run with a relatively small time step of 1 s, and it required 4380 s day^{-1} of simulation on 256 computational cores. The ADCIRC model wall-clock times reduce linearly as the number of cores is increased (Kubatko et al. 2009).

3. River validation

The representation of the Mississippi River in the SL15 model was validated by comparing measured and

predicted stages at stations from Baton Rouge to Venice, Louisiana, shown in Fig. 9. At each station, the USACE-MVN has measured stage–flow data, where water level is matched with the flow rate upriver at Tarbert Landing. Using data from multiple years, a best fit stage–flow curve can be derived at each station, as shown in Fig. 10.

SL15 model stage–flow curves, obtained by running a variety of steady flow rates on the Mississippi River, are also shown in Fig. 10. The model-predicted stages fall within the scatter of the measured data. It is only at the large flow rates that the SL15 model begins to over- or underpredict the stages. Table 10 summarizes the absolute average differences between the SL15 model stages and the measured data-derived best-fit curve. Table 10 also includes the uncertainty in the measured data by computing the absolute differences between the measured data and the measured data-derived best-fit curve. The differences between the SL15 stages and measured data-derived best-fit curve are on the same order as the estimated uncertainties in the measured data.

4. Tidal validation

The tides are weak in the Gulf of Mexico, with mixed semidiurnal and diurnal tides on the Florida shelf up to Apalachicola, Florida; diurnally dominated tides between Panama City Beach, Florida, and Port Fourchon, Louisiana; and mixed tides again being prevalent between Point au Fer Island, Louisiana, and Port Isabel, Texas. Along all three coastlines, the dominant constituents have amplitudes that are less than 0.2–0.4 m.

SL15 modeled tides are validated by comparing them to measurement-derived data at NOAA tidal harmonic constituent stations. These stations are listed in Table 11 and span the Florida Keys to Port Isabel. In Florida and Texas, where the SL15 domain does not include inland waters, stations are selected in open water. In the regions where the SL15 model does resolve inland water bodies, stations are selected in both open water and inland. Model time histories at the selected stations are analyzed harmonically over 60 days using the 23 constituents defined in Table 12.

A comparison is made between the NOAA-measured and the SL15-computed amplitudes and phases for the seven dominant constituents in Fig. 11. Difference bands are defined at 0.025 and 0.05 m for the amplitude plots and 10° and 20° for the phases. For the 10 stations in Florida, the constituents fall very near or inside the difference bands. For the stations in the other regions, the constituents group together and only the phases of the K_2 constituent show significant differences.

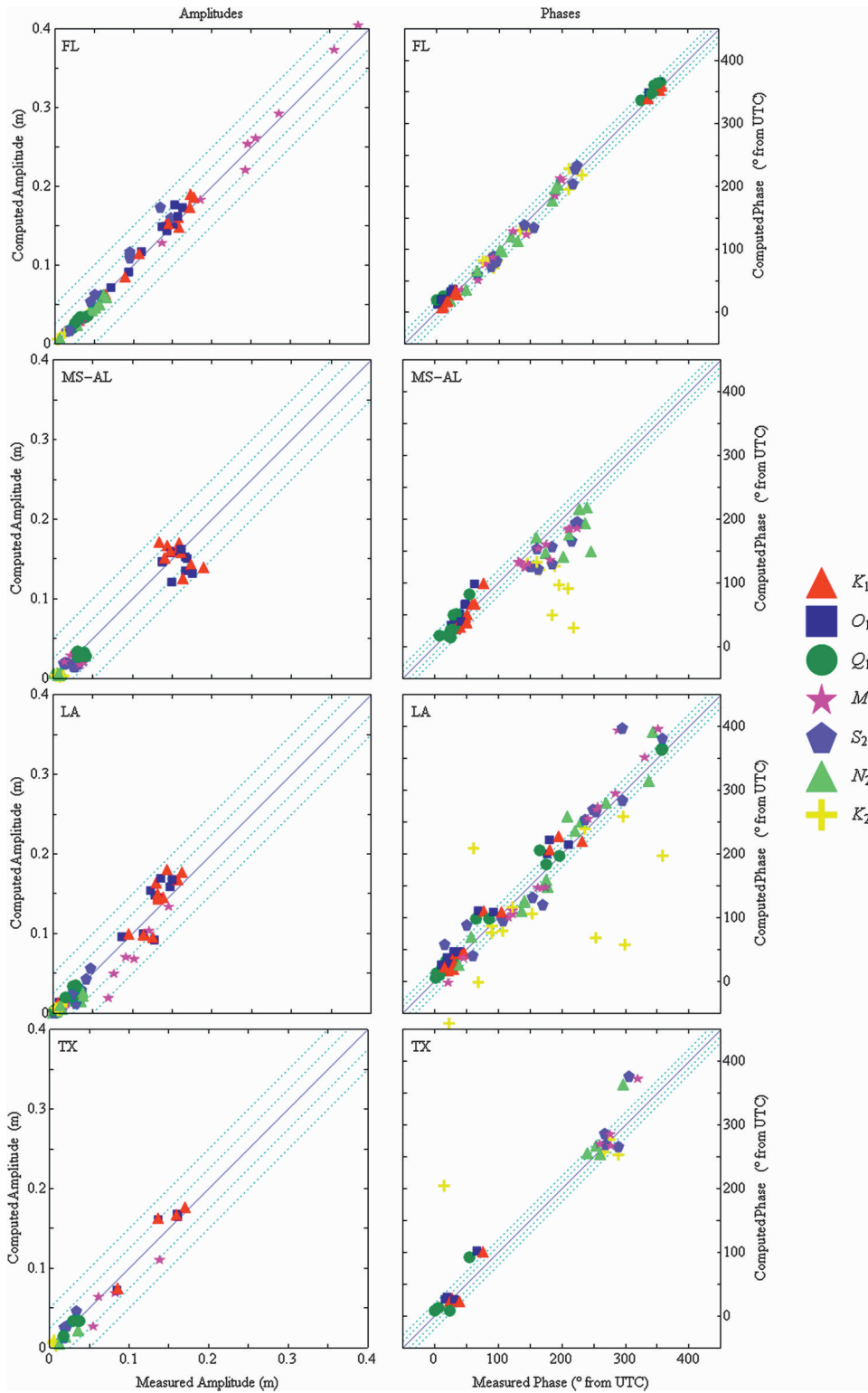


FIG. 11. Comparison of amplitudes and phases as measured by NOAA and predicted by the SL15 model: (left) amplitudes and (right) phases. Each row of figures represents a region as indicated in Table 11 with difference estimates given in Table 13.

TABLE 13. Correlation coefficients R^2 of SL15 computed harmonic constituents compared to NOAA-measured/analyzed values for the four groups of NOAA stations.

		FL	MS-AL	LA	TX
Amplitude	Seven constituents	0.991	0.953	0.947	0.962
	Six constituents (without K_2)	0.990	0.948	0.942	0.957
Phase	Seven constituents	0.993	0.768	0.839	0.896
	Six constituents (without K_2)	0.995	0.937	0.960	0.971

Table 13 lists the correlation coefficients, R^2 , for the four groups of NOAA stations. The R^2 coefficients are greater than 0.942, indicating an excellent match, with the exception of the non-Florida phases. When the K_2 constituent is removed from the analysis, these values increase to greater than 0.937. Note that the K_2 constituent is small and difficult to separate from the larger S_2 constituent in a harmonic analysis of 60 days.

Table 14 shows the difference statistics between the NOAA-measured and the SL15-computed tidal data for the four groups of NOAA stations. Average difference, average absolute difference, and the standard deviation are shown for the amplitudes and phases. In addition, the dimensionless normalized root-mean-square (rms) difference is computed for the amplitudes and is defined as

$$E_{j-\text{amp}}^{c-m} = \left\{ \frac{\sum_{l=1}^L [\hat{\eta}_j^{\text{computed}}(x_l, y_l) - \hat{\eta}_j^{\text{meas}}(x_l, y_l)]^2}{\sum_{l=1}^L [\hat{\eta}_j^{\text{meas}}(x_l, y_l)]^2} \right\}^{1/2}, \quad (1)$$

TABLE 14. SL15 model and NOAA-measured/analyzed difference statistics for the four groups of NOAA stations. These difference values include measurement uncertainties. Average, average absolute, and standard deviation amplitude differences are in m and degrees, normalized root-mean-square difference is dimensionless.

		FL	MS-AL	LA	TX	
Amplitude	Seven constituents	Avg	-0.002	0.005	0.002	0.002
		Avg absolute	0.006	0.010	0.009	0.009
		Std dev	0.009	0.014	0.013	0.012
	Six constituents (without K_2)	$E_{j-\text{amp}}^{c-m}$	0.023	0.049	0.057	0.044
		Avg	-0.003	0.005	0.002	0.002
		Avg absolute	0.007	0.011	0.010	0.010
Phase	Seven constituents	Std dev	0.010	0.015	0.014	0.013
		$E_{j-\text{amp}}^{c-m}$	0.023	0.049	0.057	0.043
		Avg	0.81	19.64	0.97	-15.70
	Six constituents (without K_2)	Avg absolute	8.54	26.19	26.20	24.97
		Std dev	10.33	38.63	46.72	42.04
		Avg	-0.36	10.54	-7.48	-12.38
	Avg absolute	7.96	17.97	18.11	19.27	
	Std dev	9.61	23.62	24.50	24.67	

where L is the number of elevation stations within a region, (x_1, y_1) is the station location, $\hat{\eta}_j^{\text{computed}}(x_l, y_l)$ is the computed model elevation amplitude for constituent j , and $\hat{\eta}_j^{\text{meas}}(x_l, y_l)$ is the NOAA-measured elevation amplitude for constituent j . In Table 14, the dimensional amplitude differences range from 0.002 to 0.010 m, and the dimensionless amplitude differences range from 0.023 to 0.057. The phase differences range from 1° to 26° . The phase behavior improves when the K_2 constituent is excluded from the analysis.

We note that these quantities reflect the differences between the NOAA-measured and the SL15 model harmonic constituents and therefore include the uncertainties in the NOAA-measured data itself. To estimate the uncertainties in the NOAA-measured data, we compare the current (as of March 2007) NOAA-published harmonic data to previously measured and published NOAA harmonic constituent data. The normalized rms amplitude and absolute average phase differences in the NOAA data at stations with multiple measured values are listed in Table 15. Overall the normalized rms amplitude differences range between 0.013 and 0.041, the average phase differences range between 5.8° and 18.4° . The measurement data uncertainties estimated by the differences between the two NOAA datasets can be explained by the shifting geometry-bathymetry of coastal regions and the occurrences of nontidal events including wind-driven events, radiational heating cycles, and riverine discharges. The measurement uncertainties represent 35%–60% of the model-to-measurement amplitude differences for the majority of the constituents. For the model-to-measurement phase differences, the measurement uncertainties account for 50%–80%. The results in

TABLE 15. Summary of SL15-computed and NOAA measurement–analysis differences for each harmonic constituent and NOAA-measured/analyzed data uncertainty estimates.

	Constituent	SL15-computed and NOAA-measured/analyzed diff	Estimated NOAA-measured/analyzed data uncertainties
Normalized rms constituent amplitude diff	K_1	0.041	0.019
	O_1	0.038	0.020
	Q_1	0.045	0.032
	M_2	0.036	0.013
	S_2	0.064	0.015
	N_2	0.076	0.031
Avg absolute constituent phase diff	K_2	0.084	0.041
	K_1	7.62	5.81
	O_1	11.84	9.38
	Q_1	10.32	6.37
	M_2	18.64	16.64
	N_2	24.19	11.75
	N_2	22.46	18.37
	K_2	60.16	11.06

Table 15 indicate that a significant portion of the difference between the model and the measurement data can be attributed to uncertainties in the measurements themselves.

5. Hurricane Katrina validation

Hurricane Katrina is incomparable in U.S. recorded events in terms of surge levels and the quality and

quantity of recorded data. Wind, wave, and water level data were collected during the event, and extensive postevent surveys of HWMs were made and referenced to NAVD88 (2004.65).

Wind speed and direction data collected during Hurricane Katrina at 12 NDBC buoys, shown in Fig. 12, are used to validate the IOKA–H*WIND wind fields. It should be noted that the NDBC buoy data are assimilated into the IOKA–H*WIND analysis, but that many other sources of data also influenced the analysis.

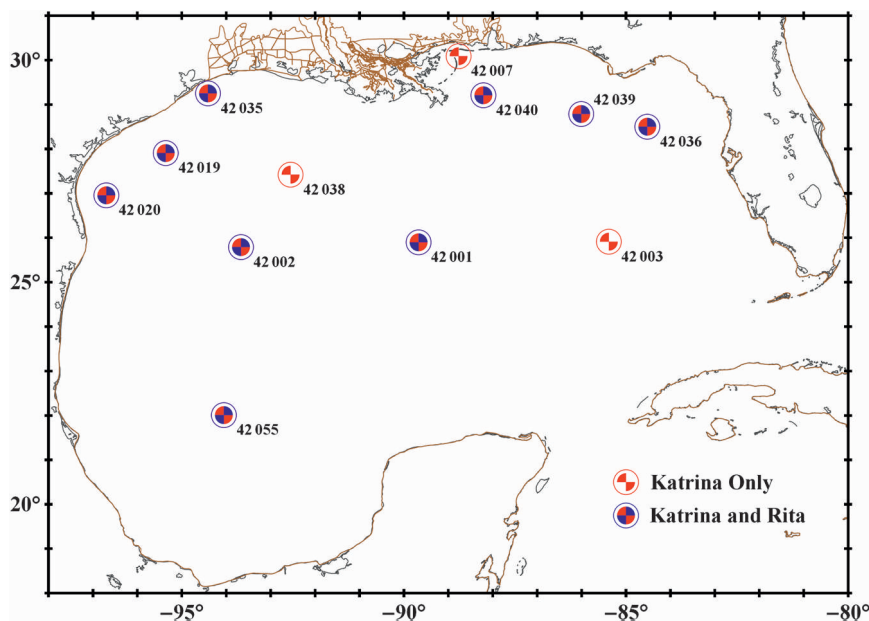


FIG. 12. Locations of the deep-water NDBC buoys used in the analysis of Hurricanes Katrina and Rita with offshore buoy identifier numbers.

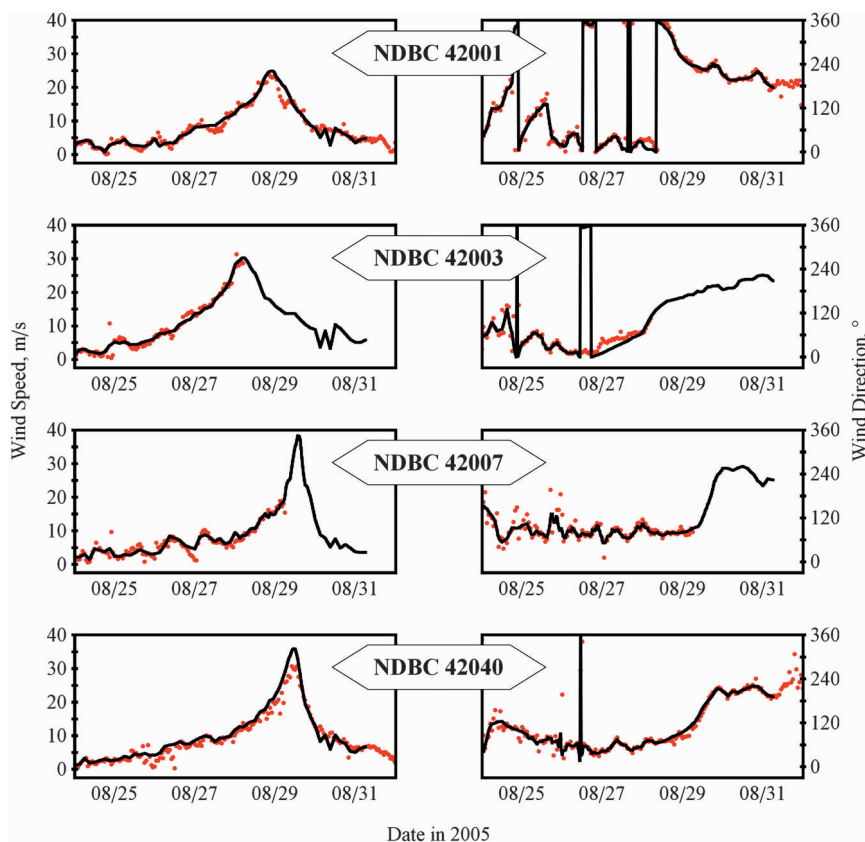


FIG. 13. Wind speeds and directions during Hurricane Katrina at four offshore NDBC buoys with buoy identifiers. The measured data is shown with red dots, while the predicted results are shown with black lines.

Differences between the IOKA-H*WIND wind and that measured at the buoys is indicative of the analysis fidelity to all the input data. Comparisons at buoys close to the storm track are shown in Fig. 13. The IOKA-H*WIND winds match the oscillations in the wind speeds before the storm, the magnitude of the peak winds, and the rate at which the winds die down after the storm passes the buoys. A one-to-one comparison of available peak wind speeds at 11 buoys shows a best-fit slope of 0.99 and an R^2 value of 0.93, indicating a good match between measured and predicted data.

At the same buoys, significant wave heights and peak wave periods are used to validate the WAM model as shown in Fig. 14. WAM matches the timing and magnitude of the peaks at the selected buoys, and a one-to-one comparison of peak significant wave heights at all 12 deep-water buoys shows a best-fit slope of 0.93 and an R^2 value of 0.90. Station 42040 misses the quick peak at this buoy as do other wave models. It is unclear if the wind fields are regionally missing features, the models are

unable to achieve the maximum wave heights or if the buoy data is biased for the two peak data points at this station. The results of the frequency spectra and the mean wave direction as a function of frequency comparisons have similar trends. Matching energy levels and mean wave directions across the entire frequency range for all NDBC sites show differences that are consistent with the peak data as well as with other third-generation wave models. We note that the peak significant wave height is the square root of the integrated energy spectrum.

STWAVE is validated by comparing computed significant wave heights and peak wave periods to limited measured data at two open-water Louisiana State University (LSU) Coastal Studies Institute stations: CSI05, located south of Isle Dernieres; and CSI06, located south of Timbalier Island (see online at <http://wavcis.csi.lsu.edu/csi05.asp?table=WCIS05> and <http://www.wavcis.lsu.edu/csi06.asp?table=WCIS06>). Comparisons at these two coastal stations are also presented in Fig. 14. At CSI05, the computed wave heights and periods match the qualitative

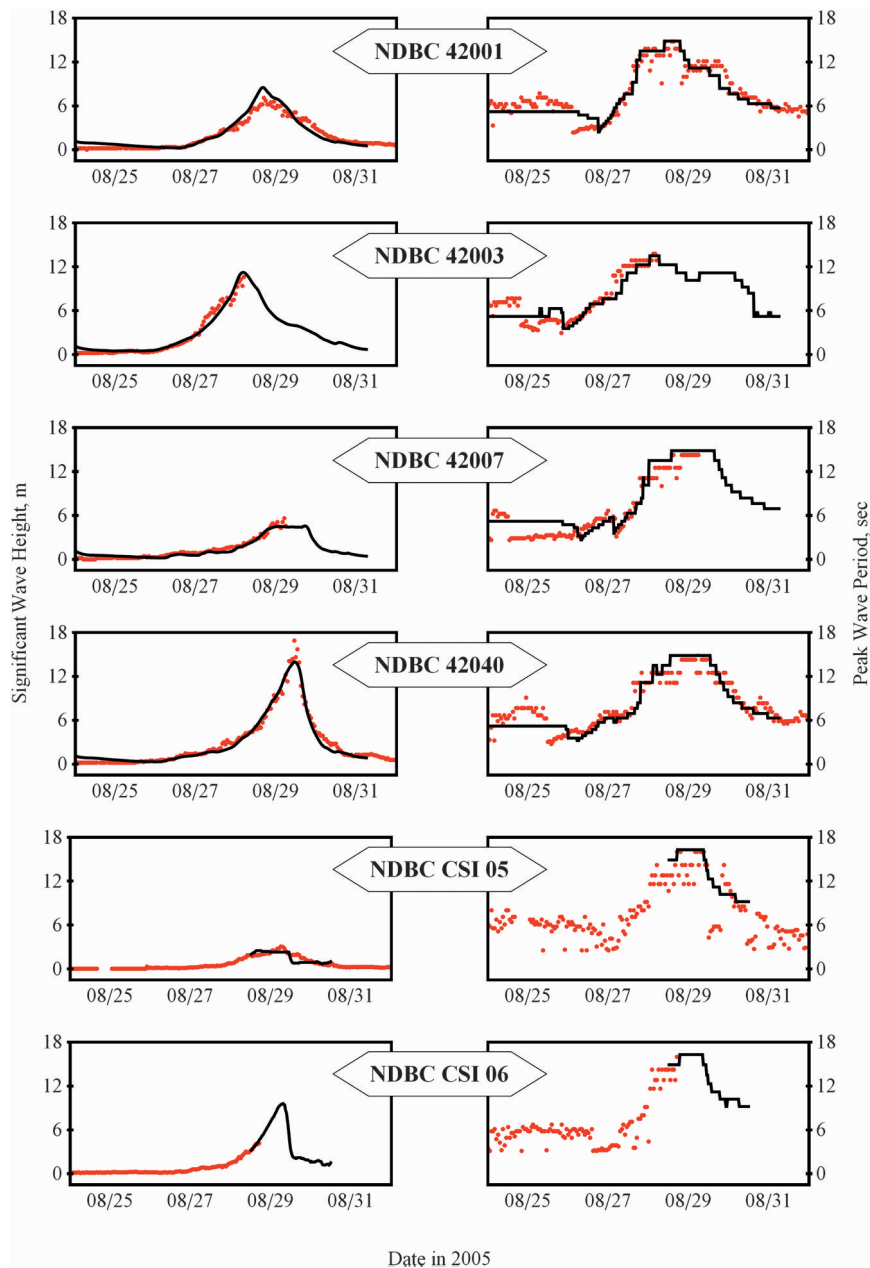


FIG. 14. Wave heights and periods during Hurricane Katrina at six NDBC buoys with identifiers. The measured data is shown with red dots, while the predicted results are shown with black lines. The first four rows show comparisons to WAM results at selected offshore buoys, while the last two rows show comparison to STWAVE results at available coastal stations.

behavior of the storm, and their values lie within the scatter of the recordings. At CSI06, where the station failed during the peak of the storm, the computed wave heights and periods match the run-up to the storm.

During Katrina, the USACE-MVN, NOS, and NWS collected hydrograph data at nine stations shown in Fig. 15. This figure also shows the differences between

ADCIRC computed and measured peak surge values at these stations. Figure 16 compares ADCIRC computed water levels against the measured time histories. Water levels at Pass Manchac on the west side of the lake compare to within 0.37 m of the measured values, showing excellent agreement in terms of timing and hydrograph features. The comparison at Bayou

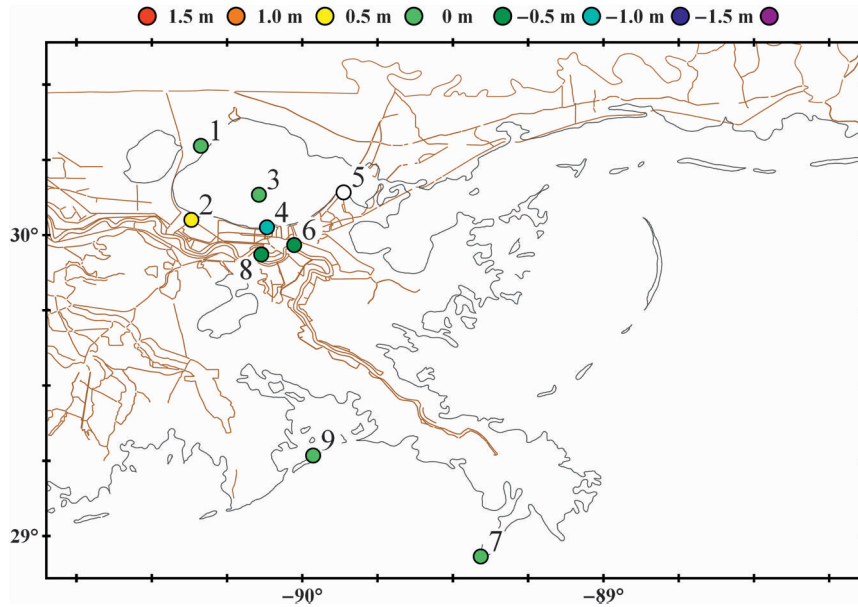


FIG. 15. Locations of the nine USACE, NOS, and NWS stations with hydrograph data for Hurricane Katrina. The nine stations are 1) Pass Manchac, 2) Bayou LaBranche, 3) Lake Pontchartrain Midlake Causeway, 4) 17th Street Canal, 5) Little Irish Bayou, 6) the IHNC Lock Staff Gauge, 7) Southwest Pass, 8) Mississippi River at Carrollton, and 9) Grand Isle. Colors indicate the differences between the modeled and measured peak surge. Green points indicate a match within 0.5 m. Red, orange, yellow, and light green circles indicate over-predictions by the model; green, blue, dark blue, and purple circles indicate underpredictions. The clear circle at station 5 indicates an incomplete hydrograph that does not allow for a peak point comparison.

LaBranche shows good agreement in the timing of peaks and rising and drainage rates. The discrepancy, which is consistent in time, is attributed to a discrepancy in datum levels. Model results at Midlake in Lake Pontchartrain show two peaks occurring in the lake. The first peak is caused by winds from the north and northeast that pile water against the lake's south shore, and the second peak is caused by the westerly winds pushing water toward the east side of the lake coupled with the massive intrusion of water from Lake Borgne during the storm's second landfall. The comparison at the 17th Street Canal indicates that the model is underpredicting peak surge by about 0.6 m, but local Boussinesq models have indicated that there is more wave-driven setup, as much as 0.5 m, which cannot be captured with the current horizontal resolution. The model results at Little Irish Bayou on Lake Pontchartrain show rising water levels that match the recorded levels. Model and measured data at the Inner Harbor Navigation Canal (IHNC) lock staff gauge at the south end of the IHNC are well matched in terms of peak water levels and drawdown rates. The model does show a temporary drawdown prior to a second peak that is not fully matched in the data. This relates to

localized drawdown on the west end of Lake Borgne that occurs as the storm passes, coupled with the model underprediction seen on the south side of Lake Pontchartrain. The comparison at Southwest Pass indicates that the modeled tides are well represented in the region and that the peak storm surge is over-predicted by about 0.4 m. The gauge at Carrollton adjacent to New Orleans indicates that the model captures the propagation of tides and surge up the Mississippi River. Finally, the comparison at Grand Isle shows good agreement. We note the excellent comparison of modeled and measured recession rates for stations in the Lake Pontchartrain–Lake Maurepas region, suggesting that the nonforced, but frictionally dominated recession process is well represented as water is withdrawn from these bodies through the Rigolets, Chef Menteur, and through Lake Borgne and off the shelf past the barrier islands.

The USACE collected 206 reliable HWMs and URS/Federal Emergency Management Agency (FEMA) collected 193 reliable HWMs during poststorm surveys with the locations and model to measurement differences shown in Figs. 17–18, respectively (Ebersole et al. 2007; URS 2006a). The HWMs were collected as

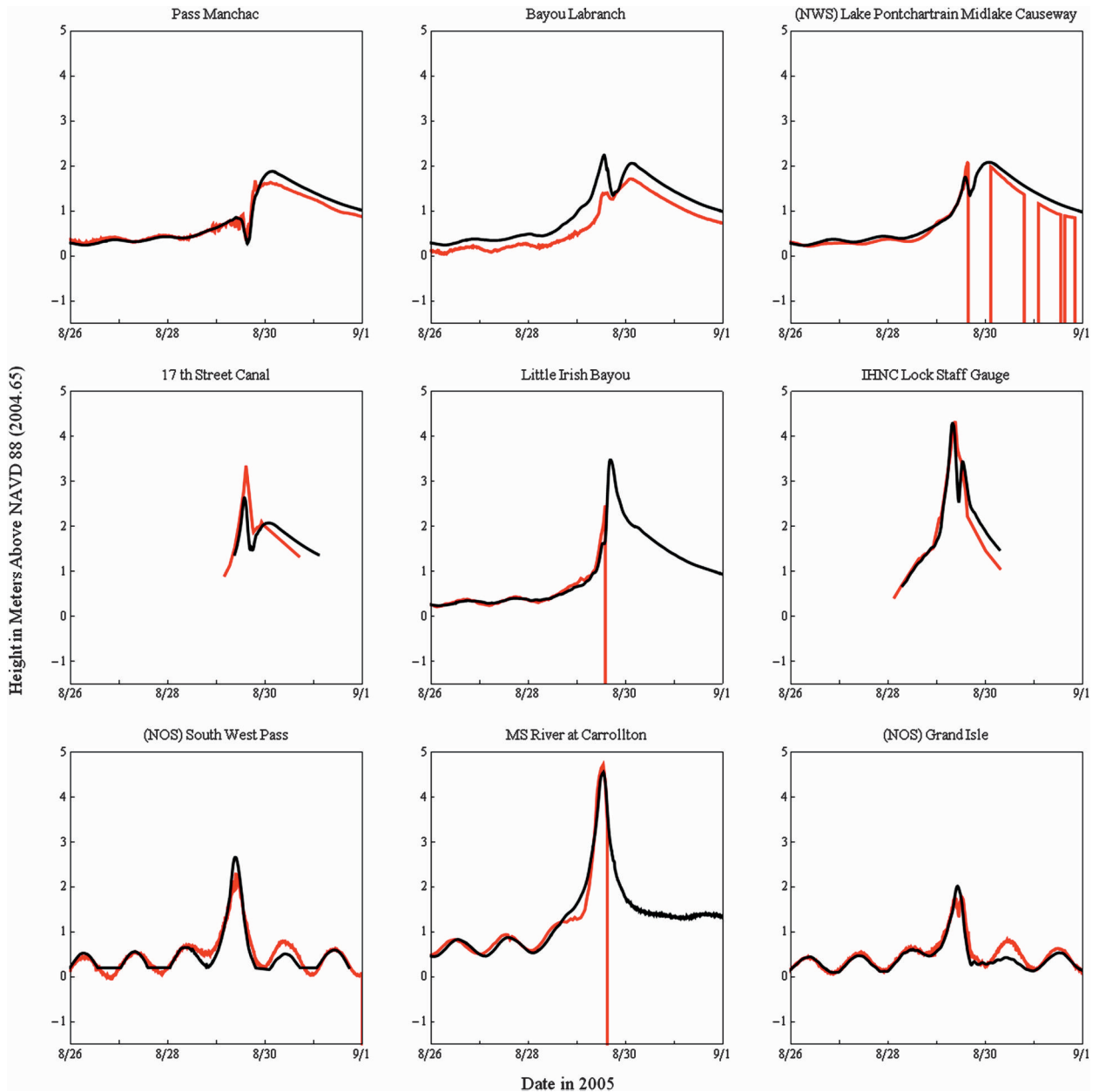


FIG. 16. Hydrographs for the nine USACE, NOS, and NWS stations during Hurricane Katrina. The black lines are the computed water levels from the ADCIRC SL15 model, while the red lines are the measured data.

indicators of the “still-water levels” and thus did not include the active motion of wind waves but did include the effects of wave setup. The two sets of HWMs offer wide coverage of the impacted region. The overall match is good, with 70% of the USACE HWMs and 73% of the URS/FEMA HWMs matching the model results to within 0.5 m. Missing features, processes, and/or poor grid resolution are associated with the larger differences. For example along the west bank of the

Mississippi River within Plaquemines Parish at Socola, Louisiana, as well as up and down river from this location, numerous HWMs within the levee system are substantially underpredicted because of the fact that we do not model levee breaching. Inadequate resolution in the circulation and wave models leads to the underprediction of wave induced setup on the south shore of Lake Pontchartrain as well as other locations with levees and raised roads. Farther inland, the model over-

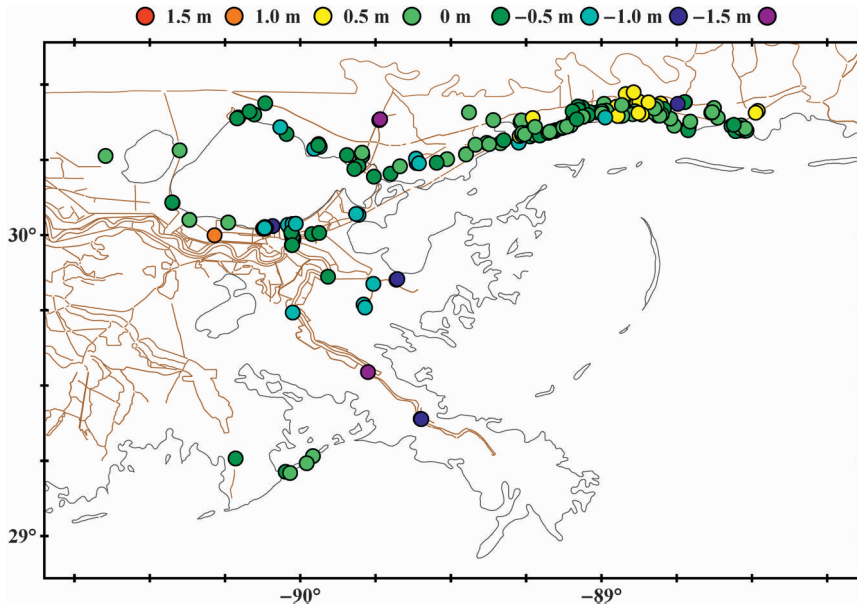


FIG. 17. Locations of USACE HWMs for Hurricane Katrina. Colors indicate the difference between the maximum computed water elevation from the ADCIRC SL15 hindcast and the measured high water mark. Green points indicate a match within 0.5 m. Red, orange, yellow, and light green circles indicate overpredictions by the model; green, blue, dark blue, and purple circles indicate underpredictions.

underpredicts surge unless the area is connected to well-defined inland waterways, which allow surge to flow past or to the HWM locations. For far inland locations adjacent to steep topography, such as up the Pearl River

basin, rainfall runoff may have significantly added to the surge levels.

Scatterplots of measured versus predicted HWMs are presented in Figs. 19–20. For the USACE marks, the

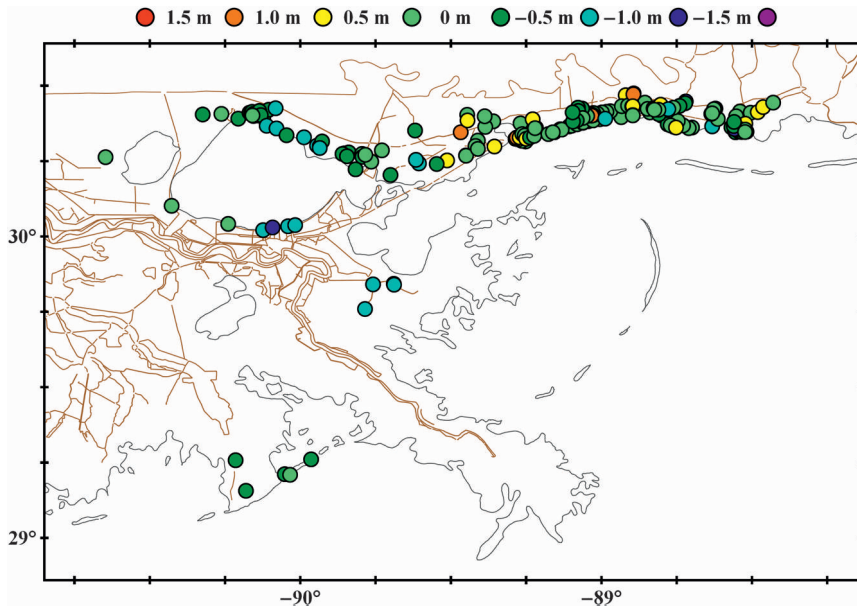


FIG. 18. As in Fig. 17, but for locations of URS HWMs for Hurricane Katrina.

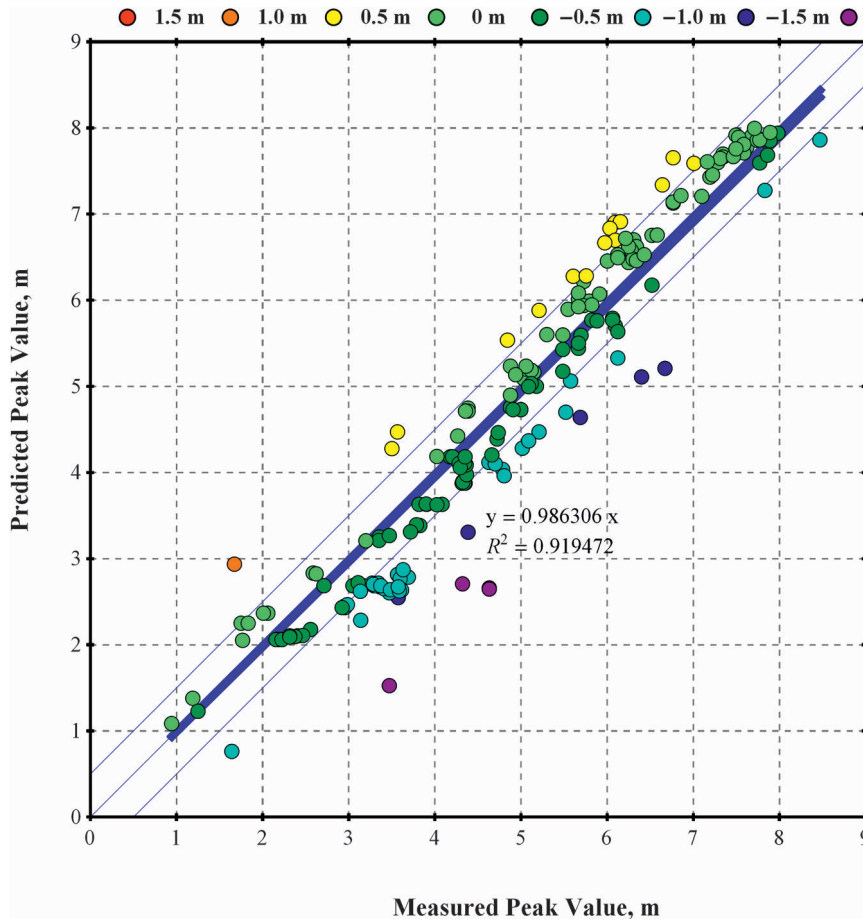


FIG. 19. Comparisons between observed USACE high water marks and ADCIRC maximum surges during Hurricane Katrina at 206 locations shown in Fig. 17. Green points indicate a match within 0.5 m. Red, orange, yellow, and light green circles indicate overpredictions by the model; green, blue, dark blue, and purple circles indicate underpredictions. The slope of the best-fit line through all points is 0.99 and R^2 value is 0.92.

slope of the best-fit line is 0.99 and the correlation coefficient R^2 is 0.92. For the URS marks, the slope of the best-fit line is 1.02 and R^2 equals 0.94. Error statistics for Katrina are summarized in Table 16. For both datasets, the average absolute difference between modeled and measured HWMs is 0.36–0.4 m, and the standard deviation is 0.44–0.48 m. A portion of these differences can be attributed to uncertainties in the measured HWMs themselves. If two or more measured HWMs are hydraulically connected (defined as being within 500 m horizontally, having no barrier in between them, and having computed water levels within 0.1 m), then HWM uncertainties are estimated by examining the differences in these adjacent HWMs. Table 16 indicates that the estimated uncertainties in the measured HWMs are 20%–30% of the differences between the modeled and measured HWMs. When the HWM uncertainties are

removed from the predicted to measured differences, then the estimated average absolute model error range is between 0.27 and 0.28 m, and the standard deviation is 0.42–0.44 m.

6. Hurricane Rita validation

Hurricane Rita was a large storm that made landfall at the western edge of Louisiana, with extensive inland penetration. Rita was also rich in both the quality and quantity of recorded data.

Wind data was collected at nine NDBC buoys shown in Fig. 12. Comparisons of wind speeds and directions at selected buoys are shown in Fig. 21. The IOKA winds match the oscillations in the wind speeds before the storm, the magnitude of the peak winds, and the rate at which the winds die down after the storm passes the

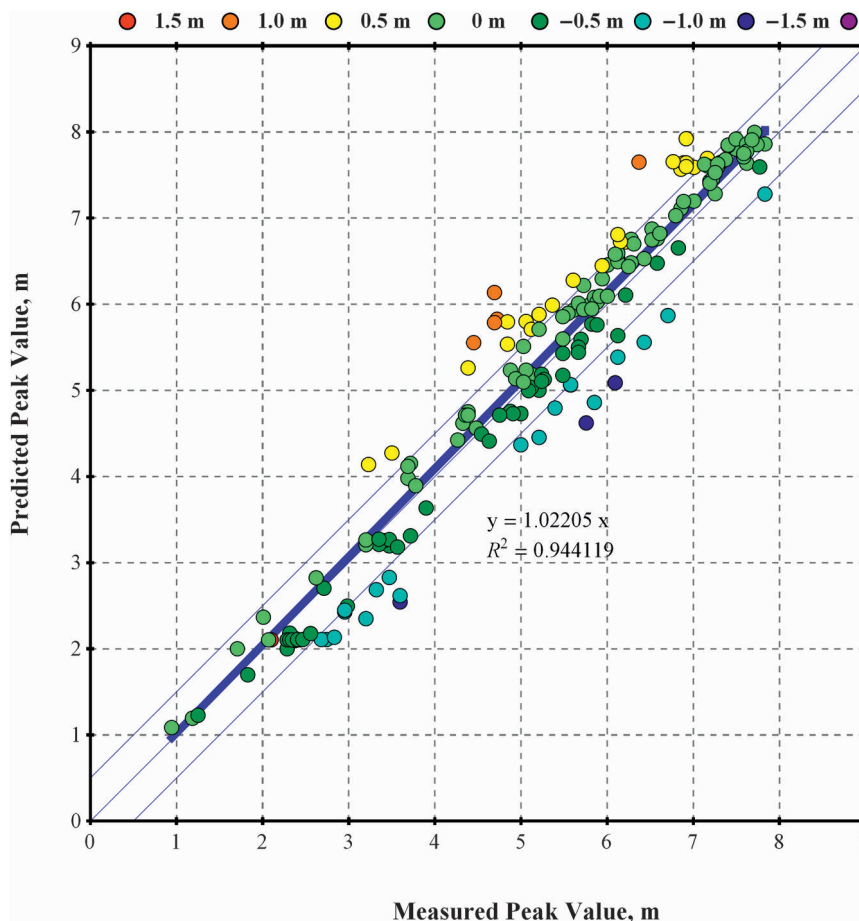


FIG. 20. As in Fig. 19, but for comparisons between observed URS high water marks and ADCIRC maximum surges during Hurricane Katrina at 193 locations shown in Fig. 18. The slope of the best-fit line through all points is 1.02 and R^2 value is 0.94.

buoy. The IOKA winds performed similarly at the other buoys, and a one-to-one comparison of peak wind speeds shows a best-fit slope of 0.97 and an R^2 equal to 0.96.

At those same deep-water buoys, the significant wave heights and peak wave periods are used to validate WAM, and time series plots at selected stations are shown in Fig. 22. WAM matches the timing and magnitude of the peaks at the buoys, and a comparison of measured and predicted peak significant wave heights at the available nine stations shows a best-fit slope of 0.96 and an R^2 value of 0.87.

STWAVE is validated by comparing its computed significant wave heights and peak periods to measured data at coastal station CSI05. As shown in Fig. 22, the model-predicted wave heights and periods lie within the scatter of the recordings. STWAVE computes a “double peak” in the wave heights and periods, because the winds shifted from southeasterly to southwesterly as Rita passed this station.

The USGS collected hydrograph data from 23 water-level sensors positioned as shown in Fig. 23 (McGee et al. 2006). This figure also shows the differences

TABLE 16. Summary of difference/error statistics for the Katrina HWM datasets. Average absolute differences/errors and standard deviations are given in meters.

Dataset	ADCIRC to measured HWMs		Measured HWMs		Estimated ADCIRC errors	
	Avg absolute diff	Std dev	Avg absolute diff	Std dev	Avg absolute error	Std dev
USACE	0.40	0.48	0.12	0.18	0.28	0.44
URS	0.36	0.44	0.09	0.15	0.27	0.42

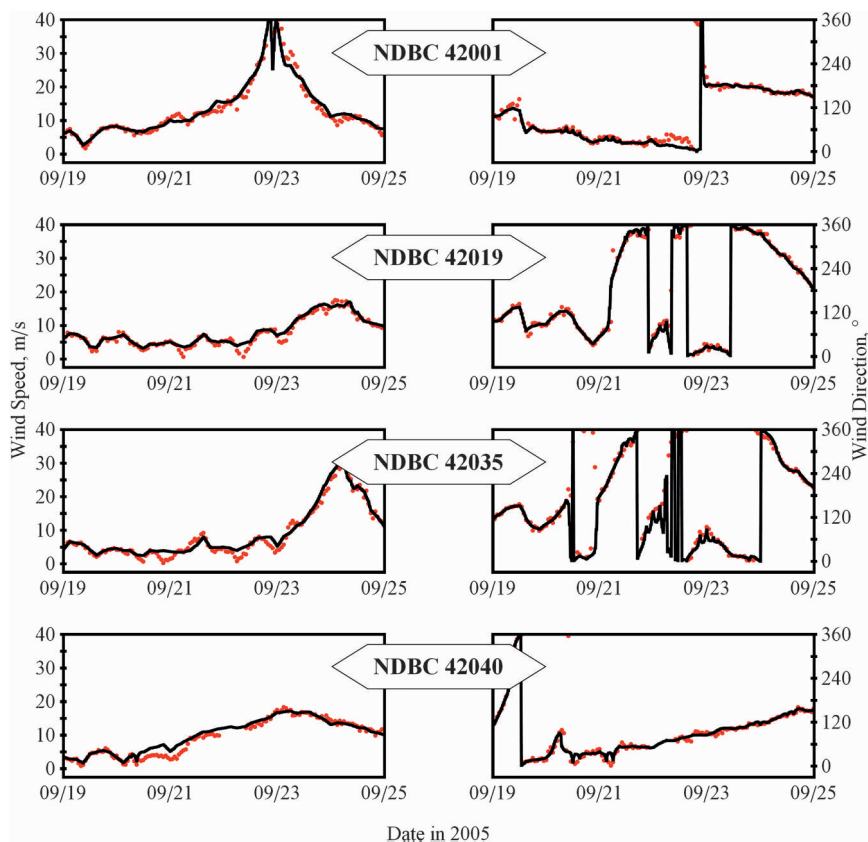


FIG. 21. Wind speeds and directions during Hurricane Rita at four offshore NDBC buoys with buoy identifiers. The measured data is shown with red dots, while the predicted results are shown with black lines.

between measured and modeled peak still water levels at these sensors. The model's ability to represent the drawdown, maximum water levels, and recession is shown in the hydrographs in Figs. 24–25. Some stations, such as LA11, LA12, LC7, LC8a, LC11, and LC12, were located in regions that are normally dry, and thus only measured water levels above the vertical position at which they were placed. At most stations the features of the measured data are modeled well. At the stations where the recession curve was recorded, the modeled rate of dewatering, which is dominated by a balance between friction and water elevation gradients, is consistent with the observed rates. This indicates that bottom friction within the model provides an accurate representation of the actual role of bottom friction across these complex series of lakes and marshes. This is of critical importance to the accurate representation of inland surge decay in hurricanes such as Hurricane Rita.

At the few stations where the match is poor between the measured and predicted water levels, a lack of resolution is almost always the cause. The inlet into Sabine Pass, near station B15b, lacks the same level of hori-

zontal resolution found elsewhere in the SL15 model. In addition there are vertical referencing uncertainties at this station. Stations LA2 and LA3 do not wet in the simulation and stations LA7 and LA8 flooded too early and by too much, because they are located along small tributaries that cannot be resolved at the 50-m resolution typically used in the model. Station LF3 also has narrow channel-scale connectivity–resolution problems. The model performs well around channels when sufficient resolution is included, such as for stations LC2a and LC2b along the wider Calcasieu Shipping Channel. These stations highlight the importance of resolution, topography, and vertical datum.

The maximum water levels can also be compared to FEMA/URS HWMs (URS 2006b). This analysis uses the 80 HWMs that were due only to storm surge with wave-induced setup and deemed by URS to be of good quality. The locations and model to measurement differences of these HWMs are shown in Fig. 26. The differences are within 0.5 m at 77% of the comparison locations across the state. A scatterplot of the HWMs is shown in Fig. 27. Overall, the slope of the best-fit

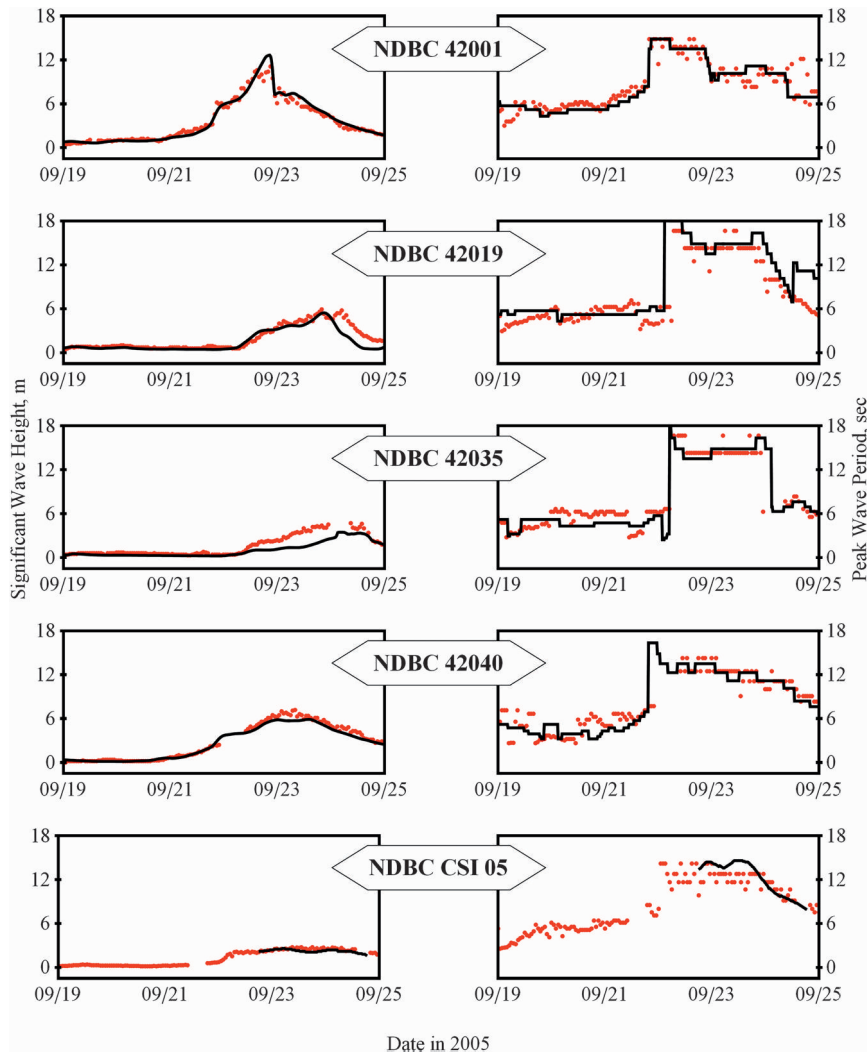


FIG. 22. Wave heights and periods during Hurricane Rita at five NDBC buoys with identifiers. The measured data is shown with red dots, while the predicted results are shown with black lines. The first four rows show WAM results at selected offshore buoys, while the last row shows STWAVE results at the available coastal station.

line through all of the scatter points is 0.97, and the R^2 is 0.77. The worst HWM comparisons are a cluster concentrated inside Vermilion Bay and are consistently underpredicted. Vermilion Bay may have problems related to the relatively low grid resolution in the region and/or its viscous muddy bottom (Sheremet et al. 2005; Stone et al. 2003), which may affect surge propagation, wind wave development and attenuation, and/or air–sea momentum transfer. A best-fit line for the 54 data points outside Vermilion Bay is presented in Fig. 28, showing a slope of 1.04, and a much improved R^2 of 0.87.

Table 17 gives the average absolute difference between modeled and measured HWMs as 0.31 m, and the standard deviation as 0.40 m. However, both quantities

improve when the HWMs near Vermilion Bay are excluded. Accounting for the uncertainty in the HWMs themselves, the estimated model average absolute errors range from 0.16 to 0.21 m with a standard deviation of 0.28–0.35 m.

7. Conclusions

Our coupled river, tide, wind, wind wave, and circulation model for southern Louisiana and Mississippi emphasizes an accurate representation of the physical features with grid resolution down to 50 m, the non-linear coupling of the multiple processes that contribute

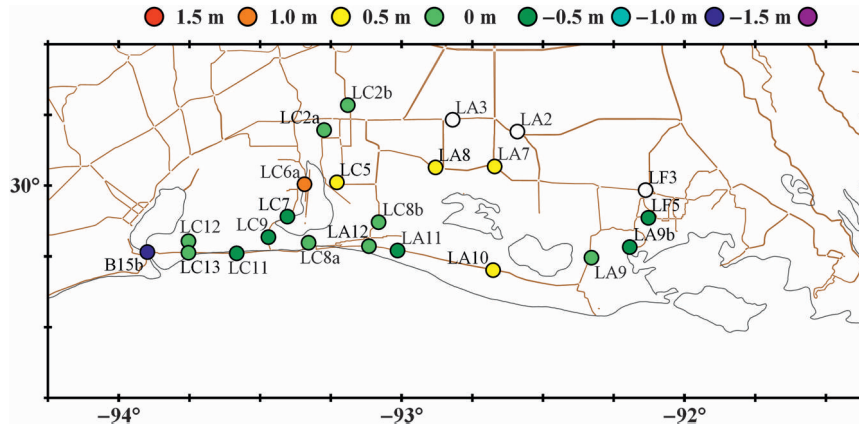


FIG. 23. Locations of the 23 USGS stations for Hurricane Rita. Colors indicate the difference between the maximum water elevation from the ADCIRC SL15 hindcast and the maximum water level from the USGS hydrograph data. Green points indicate a match within 0.5 m. Red, orange, yellow, and light green circles indicate overpredictions by the model; green, blue, dark blue, and purple circles indicate underpredictions. White points indicate stations where ADCIRC did not simulate storm surge.

to storm surge, an objective specification of frictional parameters that describe dissipation based on USGS GAP and NLCD land use data, wind adjustment based on upwind roughness, and robust and accurate boundary conditions achieved through nested model coupling in the case of the wave computations and through a basin-scale unstructured grid model for the circulation computations. Forcing functions, boundary conditions, geometric, topographic, bathymetric, and surface friction descriptors are defined within the system as they are observed and are not tuned to optimize the model to match observational data for waves or water levels.

The processes are validated separately for riverine flow and tides and concurrently for the hurricane events, validating winds, waves, hydrographs, and HWMs. Flow-stage relationships in the Mississippi River match measured best-fit relationships to within an average of 0.24 m. Tides along the Gulf Coast are also well represented by the model with the dominant diurnal tides being captured with an average absolute difference equal to 0.01 m. During the hurricane events, the kinematic wind analyses accurately represent the measured wind fields with an R^2 of 0.93–0.96 while open-water significant wave heights correlate to measured values with R^2 equal to 0.87–0.90. The HWMs during Katrina match measurements with an R^2 equal to 0.92–0.94 and after accounting for measurement data uncertainties with an estimated average absolute error of 0.27–0.28 m and a standard deviation of 0.42–0.44 m. Rita HWMs match measurements with R^2 equal to 0.77–0.87 and, after accounting for uncertainties in the measurement

data, with an estimated average absolute error of 0.16–0.21 m and a standard deviation of 0.28–0.35 m. Finally, the hydrographs demonstrate that the model captures both the forced water level rises, and flood recession process even at far inland stations, indicating that friction is correctly represented.

The ability to model waves and water levels correctly is very dependent on providing a high level of grid resolution where gradients in topography, bathymetry, geometry, forcing functions, and elevation and current response functions are significant. Topography, inlets, channels, vertical structures, wave breaking zones, and high current gradient zones all require high levels of grid resolution. Most of the poor matches to data are attributable to poor grid resolution. This includes the upper regions of the Mississippi River, wave transformation zones on the south shore of Lake Pontchartrain, Vermilion Bay, and narrow channels that penetrate roads. In addition to resolution, physical processes are critical. Riverine flows, tides, and wave-driven setup are vital contributors to overall surge. However there are additional processes that should be added to further refine model skill. Upland locations in the vicinity of steep topography may be severely underpredicted due to the lack of rainfall–runoff processes. Interior portions of levee systems also require consideration of rainfall–runoff, wave overtopping flow rates, and breaching. Vermilion Bay and other similar fine sediment deltaic regions will require a detailed examination of how muddy sea beds affect waves and surge propagation and attenuation. In addition, better descriptors of air–sea momentum transfer tied to wave conditions will be

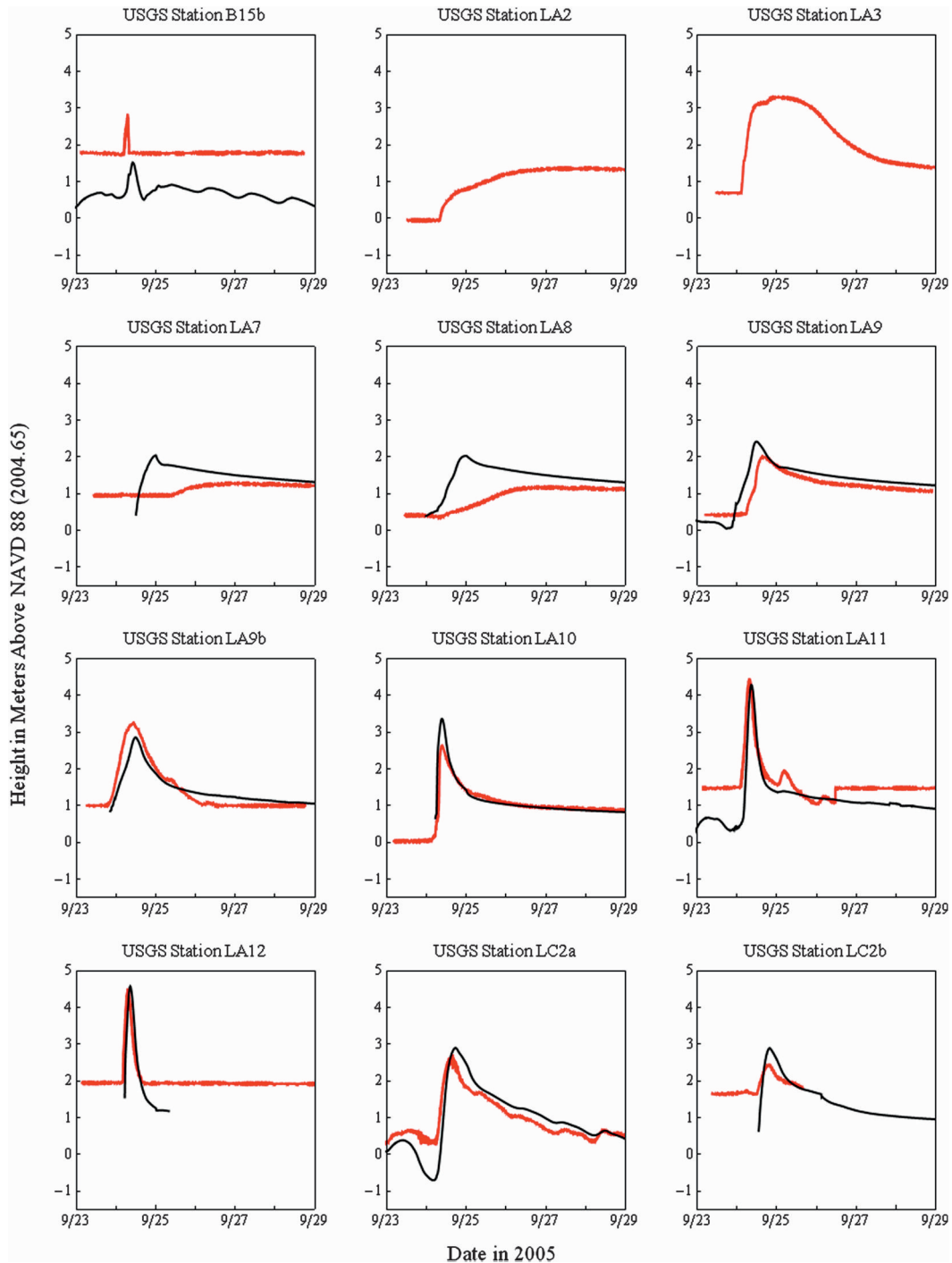


FIG. 24. Hydrographs at the first 12 USGS stations for Hurricane Rita. The black lines are the computed water levels from the ADCIRC SL15 model, while the red dots are the measured data.

beneficial. Finally vertical current structure can enhance or reduce water surface elevation.

The rapid advances in the observational systems such as lidar, satellite-based ocean vector winds and land-cover analysis, land-based and airborne Doppler radar,

airborne microwave radiometers, computational algorithms, and computing platforms will continue to allow improvements in our ability to model coastal storm environments. We envision future models focusing on higher resolution, more physics within dynamically coupled

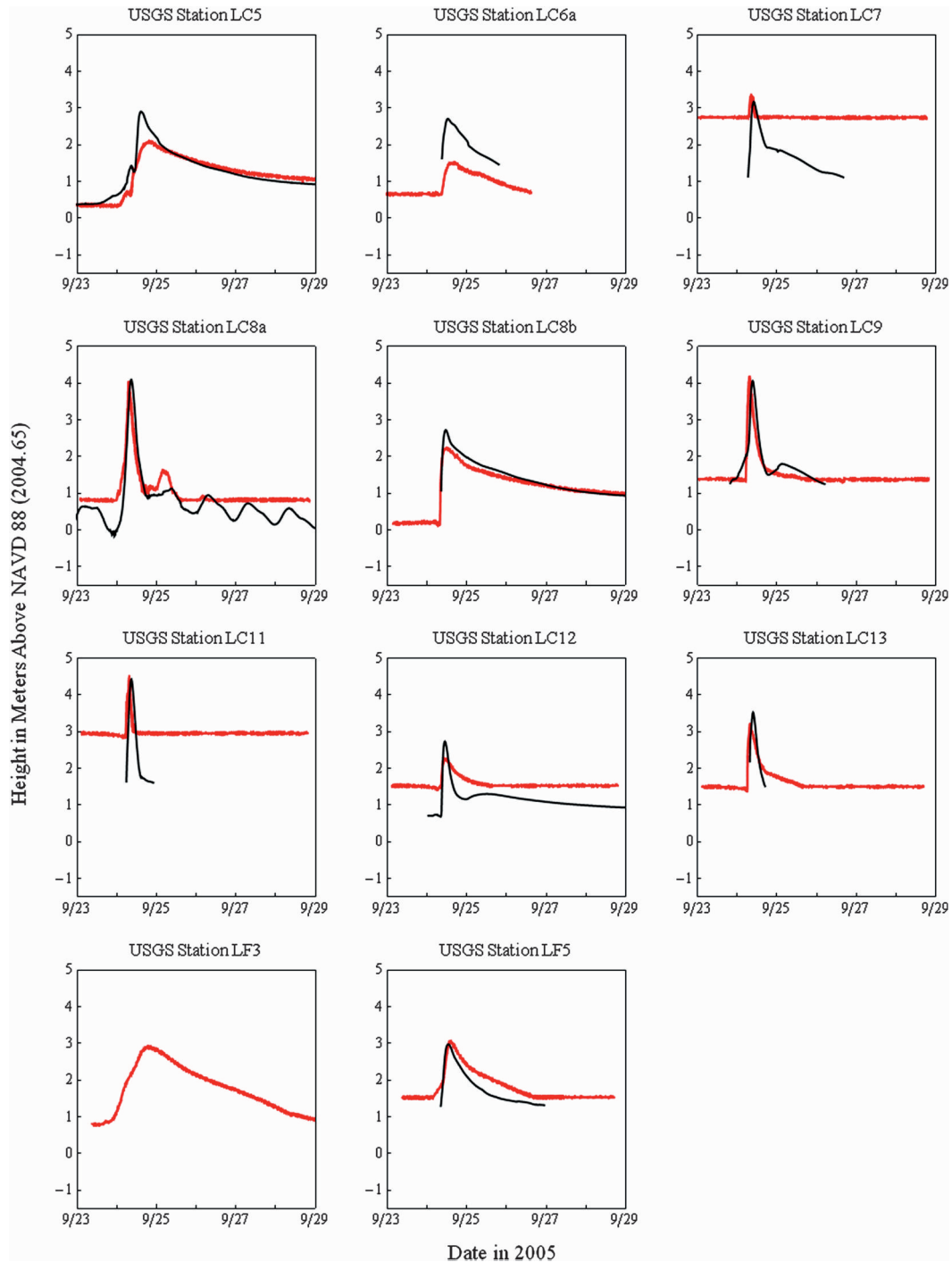


FIG. 25. As in Fig. 24, but for the last 11 USGS stations for Hurricane Rita.

systems, and improved parameterizations based on objective analyses of microscale data. Furthermore, these high-resolution hurricane models will be applied as forecasting tools using high-performance parallel computing environments.

Acknowledgments. Permission to publish this paper was granted by the Chief of Engineers, U.S. Army Corps of Engineers (USACE). This work was supported by the USACE Interagency Performance Evaluation Task Force; the Joint Coastal Surge Study in support of the

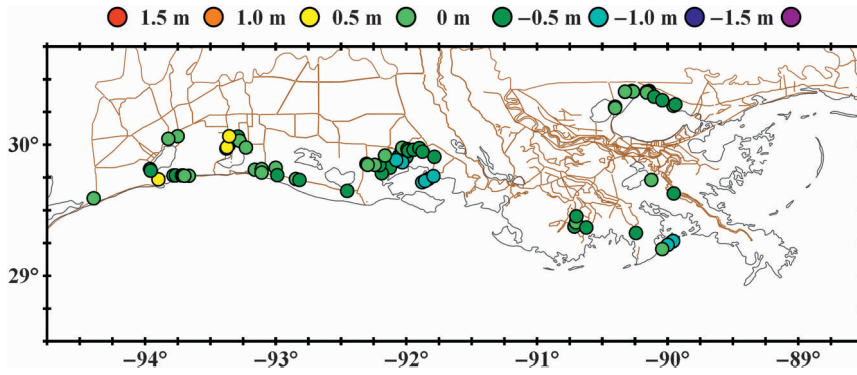


FIG. 26. Locations of the 80 HWMs obtained from URS for Hurricane Rita. Colors at each location indicate the difference between the maximum elevation from the ADCIRC SL15 hindcast and the URS HWM. Green points indicate a match within 0.5 m. Red, orange, yellow, and light green circles indicate overpredictions by the model; green, blue, dark blue, and purple circles indicate underpredictions.

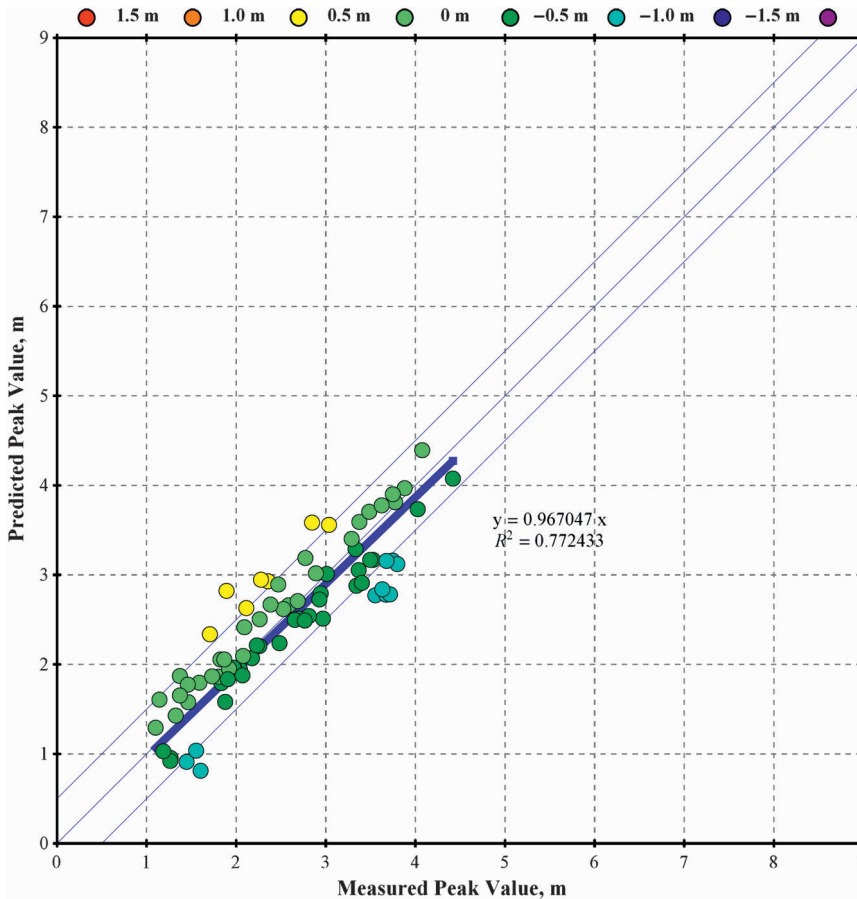


FIG. 27. Scatterplot of HWMs for Hurricane Rita. Green points indicate a match within 0.5 m. Red, orange, yellow, and light green circles indicate overpredictions by the model; green, blue, dark blue, and purple circles indicate underpredictions. The slope of the best-fit line through all points is 0.97 and the R^2 value is 0.77.

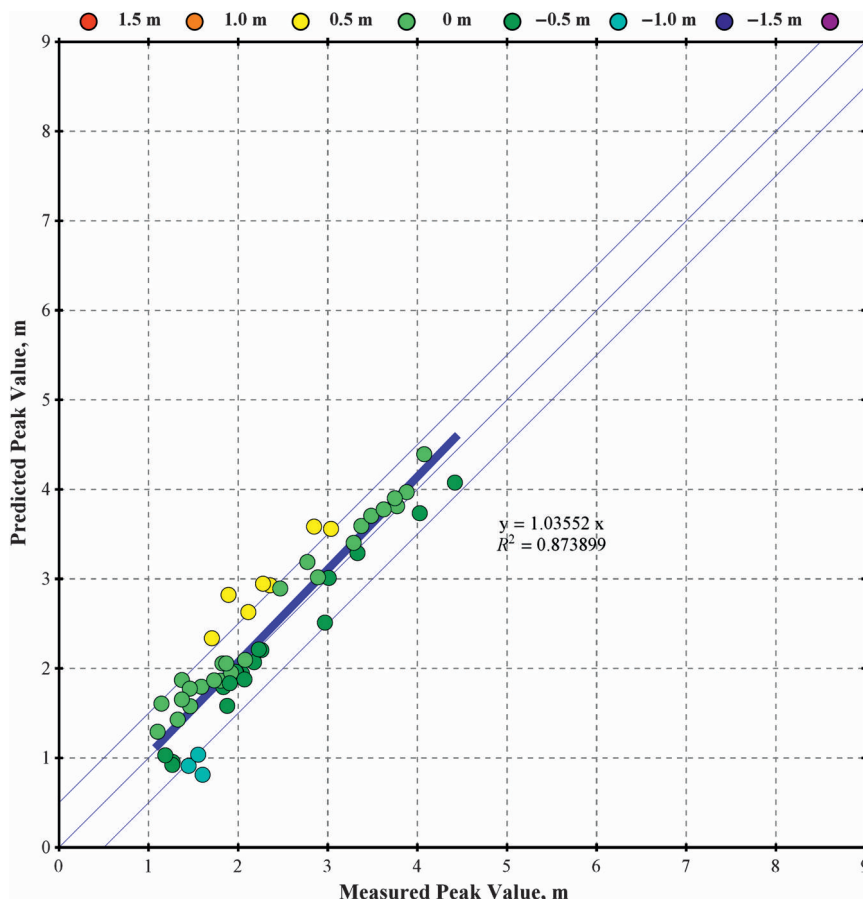


FIG. 28. Scatterplot of HWMs for Hurricane Rita without data in Vermilion Bay. Green points indicate a match within 0.5 m. Red, orange, yellow, and light green circles indicate overpredictions by the model; green, blue, dark blue, and purple circles indicate underpredictions. The slope of the best-fit line through all points is 1.04 and the R^2 value is 0.87.

USACE Louisiana Coastal Protection and Restoration Study, the USACE New Orleans District, and the USACE Hurricane Protection Office; the Federal Emergency Management Agency Region 6; and the USACE System-Wide Water Resources and MORPHOS Programs; the Department of Homeland Security Center of Excellence in Natural Hazards, Coastal Infrastructure, and Emergency Management; and the National Oceanic and Atmospheric Administration Integrated Ocean Ob-

serving System Program. Computational resources and support were provided by the U.S. Army Engineer Research and Development Center, Department of Defense Supercomputing Resource Center, and the University of Texas at Austin, Texas Advanced Computing Center. ADCIRC model development was supported by awards from the USACE, the National Science Foundation (DMS06-20696 and OCI-0746232), and the Office of Naval Research (N00014-06-1-0285).

TABLE 17. Summary of difference/error statistics for the Rita HWM datasets. Average absolute differences/errors and standard deviations are given in meters.

Dataset	ADCIRC to measured HWMs		Measured HWMs		Estimated ADCIRC errors	
	Avg absolute diff	Std dev	Avg absolute diff	Std dev	Avg absolute error	Std dev
URS	0.31	0.40	0.10	0.18	0.21	0.35
URS (without Vermilion data)	0.27	0.34	0.11	0.19	0.16	0.28

REFERENCES

- Arcement, G. J., and V. R. Schneider, 1989: Guide for selecting Manning's roughness coefficients for natural channels and flood plains. U.S. Geological Survey Water Supply Paper 2339, U.S. Geological Survey, Denver, CO, 38 pp.
- Atkinson, J. H., J. J. Westerink, and J. M. Hervouet, 2004: Similarities between the wave equation and the quasi-bubble solutions to the shallow water equations. *Int. J. Numer. Methods Fluids*, **45**, 689–714.
- Barnes, H. H., 1967: Roughness characteristics of natural channels. U.S. Geological Survey Water Supply Paper 1849, U.S. Geological Survey, Washington, DC, 213 pp.
- Blain, C. A., J. J. Westerink, and R. A. Luettich, 1994: The influence of domain size on the response characteristics of a hurricane storm surge model. *J. Geophys. Res.*, **99** (C9), 18 467–18 479.
- , —, and —, 1998: Grid convergence studies for the prediction of hurricane storm surge. *Int. J. Numer. Methods Fluids*, **26**, 369–401.
- British Oceanographic Data Centre, 2003: General Bathymetric Chart of the Oceans, Centenary Edition. [Available online at http://www.bodc.ac.uk/products/bodc_products/gebc/.]
- Cardone, V. J., and A. T. Cox, 2007: Tropical cyclone wind field forcing for surge models: Critical issues and sensitivities. *Nat. Hazards*, **51**, 29–47, doi:10.1007/s11069-009-9369-0.
- , —, and G. Z. Forristall, 2007: Hindcasts of winds, waves and currents in the northern Gulf of Mexico in Hurricanes Katrina (2005) and Rita (2005). OTC 18652, *Proc. 2007 Off-shore Technology Conf.*, Houston, TX.
- Chow, V. T., 1959: *Open-Channel Hydraulics*. McGraw-Hill Book Company, 680 pp.
- Cox, A. T., J. A. Greenwood, V. J. Cardone, and V. R. Swail, 1995: An interactive objective kinematic analysis system. *Proc. Fourth Int. Workshop on Wave Hindcasting and Forecasting*, Banff, Alberta, Canada, Atmospheric Environment Service, 109–118.
- Dawson, C., J. J. Westerink, J. C. Feyen, and D. Pothina, 2006: Continuous, discontinuous and coupled discontinuous-continuous Galerkin finite element methods for the shallow water equations. *Int. J. Numer. Methods Fluids*, **52**, 63–88.
- Dietrich, J. C., and Coauthors, 2010: A high-resolution coupled riverine flow, tide, wind, wind wave, and storm surge model for southern Louisiana and Mississippi. Part II: Synoptic description and analysis of Hurricanes Katrina and Rita. *Mon. Wea. Rev.*, **138**, 378–404.
- Ebersole, B. A., J. J. Westerink, D. T. Resio, and R. G. Dean, 2007: Performance evaluation of the New Orleans and Southeast Louisiana Hurricane Protection System, Volume IV—The storm. Final Report of the Interagency Performance Evaluation Task Force, U.S. Army Corps of Engineers, Washington, DC, 263 pp.
- Garratt, J. R., 1977: Review of drag coefficients over oceans and continents. *Mon. Wea. Rev.*, **105**, 915–929.
- Garster, J. K., B. Bergen, and D. Zilkoski, 2007: Performance evaluation of the New Orleans and Southeast Louisiana Hurricane Protection System, Volume II—Geodetic vertical and water level datums. Final Report of the Interagency Performance Evaluation Task Force, U.S. Army Corps of Engineers, Washington, DC, 157 pp.
- Gunther, H., 2005: WAM cycle 4.5 version 2.0. Institute for Coastal Research, GKSS Research Centre, Geesthacht, Germany, 38 pp.
- Hagen, S. C., J. J. Westerink, R. L. Kolar, and O. Horstmann, 2001: Two dimensional unstructured mesh generation for tidal models. *Int. J. Numer. Methods Fluids*, **35**, 669–686.
- Hartley, S., R. Pace III, J. B. Johnston, M. Swann, C. O'Neil, L. Handley, and L. Smith, 2000: A GAP analysis of Louisiana: Final report and data. U.S. Department of the Interior, U.S. Geological Survey, Lafayette, LA, 588 pp.
- Hendershott, M. C., 1981: Long waves and ocean tides. *Evolution of Physical Oceanography*, B. A. Warren and C. Wunsch, Eds., MIT Press, 292–341.
- Holland, G., 1980: An analytic model of the wind and pressure profiles in hurricanes. *Mon. Wea. Rev.*, **108**, 1212–1218.
- Kalnay, E., and Coauthors, 1996: The NCEP/NCAR 40-Year Reanalysis Project. *Bull. Amer. Meteor. Soc.*, **77**, 437–471.
- Komen, G., L. Cavaleri, M. Donelan, K. Hasselmann, S. Hasselmann, and P. A. E. M. Janssen, 1994: *Dynamics and Modeling of Ocean Waves*. Cambridge University Press, 560 pp.
- Kubatko, E. J., S. Bunya, C. Dawson, J. J. Westerink, and C. Mirabito, 2009: A performance comparison of continuous and discontinuous finite element shallow water models. *J. Sci. Comput.*, **40**, 315–339.
- Le Provost, C., F. Lyard, J. Molines, M. Genco, and F. Rabilloud, 1998: A hydrodynamic ocean tide model improved by assimilating a satellite altimeter-derived data set. *J. Geophys. Res.*, **103**, 5513–5529.
- Louisiana State University, cited 2004: Louisiana Lidar. [Available online at <http://atlas.lsu.edu/lidar/>.]
- Luettich, R. A., and J. J. Westerink, 2004: Formulation and numerical implementation of the 2D/3D ADCIRC finite element model version 44.XX. 74 pp. [Available online at http://adcirc.org/adcirc_theory_2004_12_08.pdf.]
- Mississippi Automated Resource Information System, cited 2006: Mississippi Island 10 meter by 10 meter DEM. [Available online at <http://www.maris.state.ms.us/HTM/DownloadData/DEM.html>.]
- McGee, B. D., B. B. Goree, R. W. Tollett, B. K. Woodward, and W. H. Kress, 2006: Hurricane Rita surge data, southwestern Louisiana and southeastern Texas, September to November 2005. U.S. Geological Survey Data Series 220. [Available online at <http://pubs.water.usgs.gov/ds220/>.]
- Mukai, A., J. J. Westerink, R. Luettich Jr., and D. Mark, 2002: Eastcoast 2001: A tidal constituent database for the Western North Atlantic, Gulf of Mexico, and Caribbean Sea. Tech. Rep. ERDC/CHL TR-02-24, U.S. Army Corps of Engineers, 201 pp. [Available from ERDC Vicksburg (WES), U.S. Army Engineer Waterways Experiment Station (WES), ATTN: ERDC-ITL-K, 3909 Halls Ferry Rd., Vicksburg, MS 39180-6199.]
- National Geophysical Data Center, 1988: Data announcement 88-MGG-02, digital relief of the surface of the Earth. National Oceanic and Atmospheric Administration, Boulder, CO. [Available online at <http://www.ngdc.noaa.gov/mgg/global/etopo5.html>.]
- National Ocean Service, 1997: Hydrographic survey digital database. Vol. 1, 3rd ed. National Oceanic and Atmospheric Administration.
- Powell, M., S. Houston, and T. Reinhold, 1996: Hurricane Andrew's landfall in South Florida. Part I: Standardizing measurements for documentation of surface wind fields. *Wea. Forecasting*, **11**, 304–328.
- , —, L. Amat, and N. Morrisseau-Leroy, 1998: The HRD real-time hurricane wind analysis system. *J. Wind Eng. Ind. Aerodyn.*, **77–78**, 53–64.

- Powell, M. D., P. J. Vickery, and T. A. Reinhold, 2003: Reduced drag coefficient for high wind speeds in tropical cyclones. *Nature*, **422**, 279–283.
- , and Coauthors, 2008: Reconstruction of Hurricane Katrina's wind fields for storm surge and wave hindcasting. *Ocean Eng.*, in press, doi:10.1016/j.oceaneng.2009.08.014.
- Resio, D. T., 2007: White paper on estimating hurricane inundation probabilities. U.S. Army Engineering Research and Development Center, Vicksburg, MS, 125 pp.
- Sheremet, A., A. J. Mehta, B. Liu, and G. W. Stone, 2005: Wave-sediment interaction on a muddy inner shelf during Hurricane Claudette. *Estuarine Coastal Shelf Sci.*, **63**, 225–233.
- Smith, J. M., 2000: Benchmark tests of STWAVE. *Proc. Sixth Int. Workshop on Wave Hindcasting and Forecasting*, Monterey, CA, Environment Canada, 369–379.
- , A. R. Sherlock, and D. T. Resio, 2001: STWAVE: Steady-state spectral wave model user's manual for STWAVE, version 3.0. USACE, Engineer Research and Development Center, Tech. Rep. ERDC/CHL SR-01-1, Vicksburg, MS, 81 pp. [Available online at <http://chl.erd.c.usace.army.mil/Media/2/4/4/erdc-chl-sr-01-11.pdf>.]
- Smith, S. J., and J. M. Smith, 2001: Numerical modeling of waves at Ponce de Leon Inlet, Florida. *J. Waterw. Port Coastal Ocean Div.*, **127** (3), 176–184.
- Stone, G. W., A. Sheremet, X. Zhang, Q. He, B. Liu, and B. Strong, 2003: Landfall of two tropical systems seven days apart along south-central Louisiana, USA. *Proc. Coastal Sediments '03*, Clearwater Beach, FL, University of South Florida/USGS/U.S. Army Corps of Engineers, 333–334.
- Thompson, E. F., and V. J. Cardone, 1996: Practical modeling of hurricane surface wind fields. *J. Waterw. Port Coastal Ocean Div.*, **122**, 195–205.
- , J. M. Smith, and H. C. Miller, 2004: Wave transformation modeling at Cape Fear River Entrance, North Carolina. *J. Coastal Res.*, **20** (4), 1135–1154.
- URS, 2006a: Final coastal and riverine high-water marks collection for Hurricane Katrina in Louisiana. FEMA-1603-DR-LA, Task Orders 412 and 419, Federal Emergency Management Agency, Washington, DC, 76 pp.
- , 2006b: Final coastal and riverine high-water marks collection for Hurricane Rita in Louisiana. FEMA-1603-DR-LA, Task Orders 445 and 450, Federal Emergency Management Agency, Washington, DC, 79 pp.
- , 2008: Mississippi coastal analysis project compiled reports of HMTAP. Task Order 18, Federal Emergency Management Agency, Washington, DC, Vol. 1, 376 pp.
- U.S. Department of Defense, 1999: Digital nautical chart. National Imagery Mapping Agency, Washington, DC.
- Villea, F. J., 2005: Mississippi GAP analysis project. GAP Analysis Bull. 13, U.S. Department of the Interior, U.S. Geological Survey. [Available online at <http://www.gap.uidaho.edu/bulletins/13/Mississippi.htm>.]
- Vogelmann, J. E., S. M. Howard, L. Yang, C. R. Larson, B. K. Wylie, and N. Van Driel, 2001: Completion of the 1990s National Land Cover Data Set for the conterminous United States from Landsat thematic mapper data and ancillary data sources. *Photogramm. Eng. Remote Sens.*, **67**, 650–652.
- Westerink, J. J., R. A. Luettich, and J. C. Muccino, 1994: Modeling tides in the Western North Atlantic using unstructured graded grids. *Tellus*, **46A**, 178–199.
- , and Coauthors, 2008: A basin-to-channel-scale unstructured grid hurricane storm surge model applied to southern Louisiana. *Mon. Wea. Rev.*, **136**, 833–864.